nature geoscience

SUPPLEMENTARY INFORMATION

DOI: 10.1038/NGEO1213

Superficial simplicity of the 2010 El Mayor-Cucapah earthquake of Baja California in Mexico

Shengji Wei[1], Eric Fielding[2], Sebastien Leprince[1], Anthony Sladen[1,6], Jean-Philippe Avouac[1], Don Helmberger[1], Egill Hauksson[1], Risheng Chu[1], Mark Simons[1], Kenneth Hudnut[1,3], Thomas Herring[4] and Richard Briggs[5]

1, Division of Geological and Planetary Sciences, California Institute of Technology, Pasadena, CA 91125, USA

2, Jet Propulsion Laboratory, California Institute of Technology, Pasadena, CA 91109, USA

3, United States Geological Survey, Pasadena, CA 91106, USA

4, Department of Earth, Atmospheric, and Planetary Sciences, Massachusetts Institute of Technology, Cambridge, MA 02139, USA

5, United States Geological Survey, Golden, CO 80225, USA

6, Geoazur, Observatoire de la Côte d'Azur, Université de Nice–Sophia Antipolis, CNRS, IRD, Valbonne, 06103 Nice Cedex 2, France.

Supplement Information

This file includes:

Seismicity analysis

The Caltech/USGS Southern California Seismic Network (SCSN) and the CICESE Baja California, Mexico Seismic Network (RESNOM) have recorded more than 10,000 earthquakes in the 2010 El Mayor-Cucapah earthquake sequence[1] (fig. S1). The sequence started with preshocks in March, and a sequence of 15 foreshocks of M>2 (up to M4.4) that occurred during the 24 hours preceding the mainshock. The foreshocks occurred along a north-south trend near the mainshock epicenter (Fig. 1). The Mw7.2 mainshock that occurred on 4th of April 2010 was followed by an aftershock sequence with average productivity as compared with a generic California aftershock sequence.

The aftershock zone, which has a length of more than 120 km, extends from the south end of the Elsinore fault zone at the US-Mexico border almost to the Gulf of California coast. The aftershocks that were relocated using the double-difference method[2] form two abutting clusters, of about equal length of 50 km each, as well as a 10 km north-south aftershock zone at the epicenter of the mainshock. The event relocations benefit from real-time waveform exchange between the two networks, and the availability of arrival time picks from the website provided by the CICESE Baja California, Mexico Seismic Network[3]. Even though the Baja data are included, the magnitude of completeness and the hypocentral errors increase gradually with distance to the south of the international border. The spatial distribution of large aftershocks is asymmetric with five M5+ aftershocks located to the south of the mainshock, but all the aftershocks to the north of the mainshock epicenter are smaller, but more numerous M4 events have been recorded. Further, the northwest aftershock cluster exhibits complex faulting on both northwest and northeast planes. Thus, the aftershocks also express a complex pattern of stress release along strike.

Geodetic analysis

Deformation of post-earthquake images relative to pre-event images is measured with an accuracy of a small fraction of the image pixel size independently of the ground displacement amplitude. Sub-pixel correlation is complementary to SAR interferometry (InSAR), also used in this study and which may fail in providing near-field measurements if strains are too high, and to field surveys that only allow measurement of surface slip where good piercing points are identified across well-localized surface ruptures. Correlation techniques, as well as InSAR, allow measurement of distributed strain. We used a pair of 2.5m ground resolution panchromatic SPOT

5 images acquired on May 26, 2009 and on April 8, 2010 covering the Sierra Cucapah area. We did not find suitable optical images of the delta area further to the southeast. There the fault trace was revealed from sub-pixel correlation of ALOS (Advanced Land Observation Satellite) phased-array L-band synthetic aperture radar (PALSAR) amplitude images. Together, these measurements reveal a fault trace that extends over about 120 km from the northern tip of the Sierra Cucapah to the Gulf of California (Fig. 2a). Horizontal surface slip was measured from serial profiles across the fault trace, with an average slip of about 2m.

We also use SAR interferometry (InSAR) to measure ground motion in the line of sight (LOS, near vertical) of the satellite[4]. We analyzed InSAR pairs from ALOS PALSAR (23.5 cm wavelength) and Envisat advanced SAR (ASAR, 5.6 cm wavelength) acquired with both ascending (satellite moving north and looking down to the east) and descending (satellite moving south and looking down to the west) tracks. The combination of InSAR data from ascending and descending LOS directions provides constraints on both the east and vertical components of ground displacement. Post-earthquake images were acquired between 1 and 30 days after the main shock so that some postseismic deformation might be present in the data. The coherence is generally good, except in a few areas where the landscape has significantly changed due to vegetation changes or earthquake induced landslides and liquefaction. The fringe pattern is also obscured in the near field area where the fringe rate exceeds one fringe per pixel or where coherence is lost due to too intense ground deformation. The InSAR measurements show deformation at distances between about 1 km and 100 km from the fault, thereby providing strong constraints on the distribution of slip at depth, complementing constraints from the optical and SAR pixel tracking along the surface trace in Fig. 2a.

(a) *SPOT data analysis*

Horizontal ground deformation to the north of the epicenter was retrieved using precise co-registration and sub-pixel cross-correlation of optical satellite images (Fig. 2a). The images' analysis was performed using the COSI-Corr (Co-registration of Optically Sensed Images and Correlation) software package[5]. We used a pair of 2.5m ground resolution panchromatic SPOT 5 images acquired on May 26, 2009 and on April 8, 2010, with near nadir looking angles to minimize topography parallax. The image pair has an incidence angle difference of 6 degrees and we used the 30m NED DEM for orthorectification. Slight topography residuals persist in the

East-West component but the North-South component of the deformation field, being mostly perpendicular to the epipolar direction of the image pair, is devoid of topography residuals. Image cross-correlation was performed using 64×64 pixel-windows sliding at every 16 pixels, resulting in a deformation field sampled at every 40m.

(b) ***SAR data analysis***

We formed 9 interferograms from Envisat ASAR and ALOS PALSAR scenes on 9 different satellite tracks with the post-earthquake scenes acquired between one and 30 days after the earthquake (Supplementary Tables S1-S2 and figs. S4 to S6, S8 to S11) using the JPL/Caltech ROI_pac[6] and Stanford SNAPHU[7] software (see Supplementary Information for full Methods description). In addition to the interferograms, pixel tracking analysis was performed on the full-resolution SAR image pairs to measure the along-track (roughly N-S) displacements (Fig. 2a).

Synthetic aperture radar (SAR) interferometry analysis presented here used data acquired by the Japanese Aerospace Exploration Agency (JAXA) Advanced Land Observation Satellite (ALOS), with its phased-array L-band SAR instrument (PALSAR) that has a radar wavelength of 23.5 cm, and by the European Space Agency (ESA) Envisat satellite, with its advanced SAR (ASAR) C-band instrument that has a radar wavelength of 5.6 cm. The data was processed from the PALSAR Level 1.0 and ASAR Level 0 raw data with the JPL/Caltech ROI_pac SAR interferometry package[6]. The topographic data used to calculate and remove the topographic phase was the Shuttle Radar Topography Mission (SRTM) 1-arcsecond posting digital elevation model with the data voids filled by interpolation with the ITT ENVI program. PALSAR interferograms were analyzed with averaging (looks) of 2 or 4 samples across-track and 4 or 8 samples along-track. ASAR interferograms were analyzed with averaging (looks) of 2 or 4 samples across-track and 10 or 20 samples along-track. The interferograms were unwrapped with the standard ROI_pac programs based on the Goldstein-Zebker-Werner algorithm[8] or with SNAPHU[9].

ALOS PALSAR data were processed from four satellite paths, three ascending (satellite moving northward) paths and one descending (satellite moving southward) path as shown in Table S1. ALOS data were processed with the precise orbits from JAXA. PALSAR scenes were acquired in the fine-beam single-polarization (FBS) and fine-beam dual-polarization (FBD) modes. The FBD scenes were oversampled in range to the same sample spacing as the FBS

scenes. All the PALSAR data were acquired with the standard 34.3° look angle (at the satellite) that results in line-of-sight (LOS) angles relative to the vertical at the Earth's surface varying from 36° to 41° across the radar swath. The LOS unit vector from the ground at the center of the swath to the satellite on the ascending paths is (-0.6080, -0.1337, 0.7826) for east, north, and up components, while the descending path has an LOS unit vector of (0.6080, -0.1337, 0.7826).

Table S1. ALOS PALSAR pairs used for interferograms.

ALOS path	Date1	Date2	Bperp.* (m)
A211	2010/01/15	2010/04/17	663–725
A212	2009/12/17	2010/05/04	953–1037
A213	2010/01/03	2010/04/05	538–592
D533	2009/11/30	2010/04/17	1338–1269

* Perpendicular component of baseline at center of swath from top to bottom of interferogram.

Envisat ASAR data were processed from five satellite paths, two ascending (satellite moving northward) tracks and three descending (satellite moving southward) tracks as shown in Table S2. Envisat data were processed with the ESA verified DORIS orbits (VOR) for the pre-quake scenes and the preliminary precise DORIS orbits (POR) for the post-quake scenes. ASAR scenes were acquired in image mode beam I2 that has LOS angles relative to the vertical at the Earth's surface varying from 18° to 26° across the radar swath. The LOS unit vector from the ground at the center of the swath to the satellite on the ascending tracks is (-0.3729, -0.0861, 0.9239) for east, north, and up components, while the descending tracks have an LOS unit vector of (0.3724, -0.0880, 0. 9239).

Table S2. Envisat ASAR pairs used for interferograms.

Envisat track	Date1	Date2	Bperp.* (m)
A077	2010/03/28	2010/05/02	-197–-205
A306	2010/03/09	2010/04/13	263–284

D356	2010/03/12	2010/04/16	262–217
D084	2010/03/28	2010/05/02	-98–-86
D313	2010/03/09	2010/04/13	313–279

* Perpendicular component of baseline at center of swath from top to bottom of interferogram.

To limit the number of data used in the inversion, the interferograms were downsampled to about 1000 points each using a distribution of samples optimized for determining the slip on two faults similar to the main faults (F2, F3 & F4) used in the slip inversions[10] (figs. S4 to S6).

(c) ***SAR pixel tracking***

Sub-pixel correlation on SAR image pairs was performed using the spatial domain cross-correlation program from ROI_pac[11]. The cross-correlation is done on the full-resolution focused single-look complex (SLC) image amplitudes in the radar imaging coordinates to maximize the resolution of the pixel offset calculations. A surface fit to the cross-correlation measurements allows the estimation of the peak of the cross-correlation function to about .05 to 0.2 of a pixel, depending on the match quality. The pixel offsets are estimated in both the range or cross-track direction, which measures displacements in the radar LOS like InSAR phase, and in the azimuth or along-track direction, which measures displacements in the direction of the satellite track. An estimate of the topographic and baseline components were calculated and removed from the range offsets. For the azimuth offsets, a quadratic fit to the whole scene offsets was removed to empirically remove the baseline component.

(d) ***GPS analysis***

The co-seismic displacements were determined by combining the Plate Boundary Observatory (PBO) and the United States Geological Survey (USGS) processing of the GPS data from two days before the earthquake (April 2 and 3) with two days after the earthquake (April 5 and 6). The processing used the IGS final orbits and the results, in the form of the Solution Independent Exchange (SINEX) format files, are available from the PBO data products area (ftp://data-out.unavco.org/pub/products/sinex/). Changes in the positions of 132 GPS sites within 325 km of the epicenter were estimated. The reference frame for the offsets was based on the

aligning the combination through rotation and translation of the network to the positions of 785 PBO reference sites spanning the North America and part of the Pacific plate. The coseismic offsets of the 23 GPS sites closest to the rupture were used in the inversion (fig S7). The remaining 109 coseismic offsets from the GPS analysis were not used. The GPS offsets showed up to 20cm of horizontal displacements and are consistent with dominantly right-lateral slip.

Modeling and inversion procedure

To derive finite source kinematic models, we use the method developed by[12,13] which allows the joint inversion of seismic waveforms and coseismic static displacements. As teleseismic and static data provide complementary constraints on the kinematic rupture process, we used both data sets to invert the slip history.

The determination of a finite fault slip model is an underdetermined problem due to numerous trade-off among model parameters, such as rise time and rupture velocity, when only seismic data are used. The trade-offs are significantly reduced if coseismic geodetic observations are available and inverted jointly with the seismological data. Even though, the determination of a finite fault source remains generally underdetermined if the fault discretization is too fine. One way to regularize the inversion is setting some constraints on the roughness of the slip distribution[12], which is the approach adopted here. For each subfault, we solve for the slip amplitude and direction, rise time and rupture velocity. For each parameter, we specify extremal bounds and a discretization interval. We solve for quadratic ramps in the InSAR data to correct for orbital errors that have not been removed through baseline reestimation and interseismic deformation.

We define the best fit model as having the lowest objective function, given as: E_{wf}+ W_I *E_I + W_S *S + W_w*M, where E_{wf} is the waveform misfit. E_I is the geodetic misfit, S is a normalized, second derivative of slip between adjacent patches (smoothing). M is a normalized seismic moment, and W_I, W_S and W_M are the relative weighting applied to the geodic misfit, smoothing, and moment, respectively. The least squares misfits are calculated for the teleseismic and geodetic data. Here we test different values of W_I, and we found that by setting the weight for the geodetic misfits twice larger than the waveform misfits did not significantly degrade the fits to the teleseismic or geodetic data between the individual and joint inversions given the normalizations schemes. The static green's functions at free surface are calculated by using the

same 1D standard Southern California crustal model as used in teleseismic body-wave calculation. Different smoothness values are tried in the static inversion, ranging from 1.0 to 0.0001. We do not see large changes in the solution for smoothness value smaller than 0.1, which is the value used later in the joint inversion (fig. S12).

We use a simulated annealing algorithm[14] to find the best fitting model parameters for the joint inversions for coseismic slip. This nonlinear, iterative inversion algorithm is designed to avoid local minima by searching broadly through parameter space in initial steps, and then in later iterations to focus on regions that well fit the data [15].

One of the main difficulties involves adding the normal event (F1) which is small to compete with large static offsets produced by the main fault strands. One way to do this is to examine stations that are relatively nodal for the main rupture such as the station PAB in (fig. S14). Note that the first arrival of about 15s length is only apparent at this station. Since there are a large number of seismic stations globally we are able to model the first 15s of data to obtain the mechanism of F1 (fig. S2). Although the slip-distributions for F2 and F3 are known from static inversion(fig. S3), the jump of rupture from F1 to F2 remains an issue. Two parameters involving the F2 epicenter and timing delays relative to F1 were investigated by computing the best fitting comparisons of synthetics to observed P and S waveforms as for the few P-waveform samples given fig. S2. The intersection of fault-plane F1 with F2 fits the best with location given earlier in Fig. 1. The delay between the two events is near 14s, see fig. S14 for detailed comparisons.

Here the subfault size is chosen as 3km×3km, the rake angles have been constrained to be between right lateral strike slip and normal slip, and the rupture velocity is allowed to vary between 2.0~3.0km/s, the rise time is assumed to be an arc of the cosine function, first quarter and to vary between 0.8 and 8 s with 0.8s steps. The rise-time estimates were used to construct the slip-rates per patch as given in fig. S15, by dividing the slip amplitudes by their individual rise-times. These are summed to produce the moment-rate contributions per fault as display in Fig. 3d.

Figure Captions:

Figure S1. Seismicity recorded from the Caltech/USGS Southern California Seismic Network (SCSN) and the CICESE Baja California, Mexico Seismic Network (RESNOM). Red dots show aftershocks of the 2010 El Mayor-Cucapah earthquake (between April 4th, 2010 and June 16th), black and blue circles

show seismicity recorded in 2009. Red line indicates simplified plate boundary between the Pacific and the North America plates. Blue star shows epicenter of mainshock and other beach balls are moment tensor mechanisms of some significant events before and after the El Mayor-Cucapah earthquake. The solid yellow star indicates the 24 Feb., 1892 earthquake[16]. The 1979 Imperial Valley moment tensor is from[17]. Black thin lines are known faults with the green line as the surface rupture of this earthquake.

Figure S2. Mechanism of the first event is obtained by inverting the first 15 seconds of teleseismic P-waves, the sampling points on the lower-hemisphere of beach ball are plotted as red crosses, and waveforms of representative stations are plotted in black (data) and red (synthetic) with station names on the beginning of the record.

Figure S3. Slip distribution derived from the inversion of the geodetic GPS and remote-sensing data (InSAR, SPOT offsets, SAR azimuth offsets). The first segment(F1) is ignored here.

Figure S4. Ascending InSAR sampling points used in the inversion. Date pair and satellite information is indicated above each synthetic plot, rectangle is projection of each fault segment and the star is the epicenter. Sampling points are colored by motion in the line of sight (LOS) direction, with positive representing motion away from satellite and negative for motion towards satellite. Black dots in the synthetic plot are fault trace sampling points derived from Fig. 2a. Thin black rectangles show surface projection of the idealized fault segments used in the modeling.

Figure S5. Descending InSAR sampling points used in the inversion. Refer to S4 for detail of description.

Figure S6. SAR azimuth offset sampling points used in the inversion, positive values represent horizontal motion along azimuth direction of satellite. Refer to fig. S4 for the other information.

Figure S7. Horizontal (upper left) and vertical (upper right) GPS record (black) and synthetic (red), with the star indicates the epicenter and thin black rectangles indicate surface projection of the idealized fault segments used in the modeling. The residual between data and synthetic is plotted below each component.

Figure S8. Ascending InSAR data image (left), prediction from the preferred model (middle) and the residual (right). Date pair and satellite information is indicated above each data image, rectangles are projection of fault segments and the star is epicenter. Each color cycle indicates 11.8cm of motion in the line of sight (LOS) direction.

Figure S9. Descending InSAR data image (left), prediction from the preferred model (middle) and the residual (right). Refer to S8 for detail of other information.

Figure S10, Ascending InSAR unwrapped image(left), prediction from the preferred model (middle) and the residual (right). Refer to S8 for detail of other information.

Figure S11, Descending InSAR unwrapped image (left), prediction from the preferred model (middle) and residuals (right). Refer to S8 for detail of other information.

Figure S12, Weighted error vs. smoothness coefficient for the geodetic only inversion. There is not much change in error when smoothness coefficient is less than 0.1.

Figure S13, (A) Distribution of 29 P (square) and 20 SH (inverse triangle) recordings, black (P) and red (SH) lines are paths connecting the epicenter and the representative stations. Concentric circles are shown every 30º of azimuthal distance from the epicenter. Left column in (B) and (C) is the four representative teleseismic P and SH-wave displacement (black) and synthetic (red) generated by the preferred model. The station names are indicated to the left of the traces along with the azimuths and epicentral distances in degrees. The peak amplitude in micron of data is indicated above the end of each trace. The right panel indicates the contribution of each segment with black line as the sum. Synthetic of F1 is in orange, F2 in red, F3 in green and F4 in light blue.

Figure S14. Comparison of the observed (black) and modeled (red) teleseismic seismograms (in displacement). Station names are indicated to the left of the traces along with the azimuths and epicentral distances in degrees. Peak amplitude in micron of data is indicated above the end of each trace. The first 15 seconds of COLD (in velocity) is enlarged and displayed on the top, note the small event at the very beginning.

Figure S15, Rise time(A) and slip rate(B) of the prefer model, all the isochrons of the rupture are given relative to the epicenter for F1. Strike angle is displayed below each segment in (A).

Figure S16, 3D plot of fault geometry with the arrow indicates the north direction.

Figure S17, Horizontal components of PBO P494 GPS station. The SOPAC estimate of linear velocity trend has been removed from the time series. The magenta line marks the April 4 earthquake and the green line marks the large Mw5.7 aftershock north of the border on June 15. Coseismic deformation is removed from (a) to better indicate the postseismic deformation (b).

Reference

1 Hauksson, E. *et al.* The 2010 Mw 7.2 El Mayor-Cucapah Earthquake Sequence, Baja California, Mexico and Southernmost California, USA: Active Seismotectonics along the Mexican Pacific Margin. *Pure Appl Geophys*, doi:DOI: 10.1007/s00024-010-0209-7 (2010).

2 Waldhauser, F. & Ellsworth, W. L. A double-difference earthquake location algorithm: Method and application to the northern Hayward fault, California. *Bull. Seismol. Soc. Am.* **90**, 1353-1368 (2000).

3 Vidal, A., Munguia, L., Mendez, I. & J., F. F. Seismological Bulletin from the Red Sismica Del Noroeste De Mexico. (2009).

4 Simons, M. & Rosen, P. in *Treatise on Geophyics* Vol. 3 (ed G. Schubert) 391~446 (Elsevier Press, 2007).

5 Leprince, S., Barbot, S., Ayoub, F. & Avouac, J. P. Automatic, Precise, Ortho-Rectification and Co-Registration for Satellite Image Correlation, Application to Seismotectonics. *IEEE Transactions on Geoscience and Remote Sensing* **45**, 1529-1558 (2007).

6 Rosen, P. A., Hensley, S., Peltzer, G. & Simons, M. in *EOS, Trans. AGU* Vol. 85 47 (2004).

7 Chen, C. W. & Zebker, H. A. Network approaches to two-dimensional phase unwrapping: intractability and two new algorithms. *Journal of the Optical Society of America a-Optics Image Science and Vision* **17**, 401-414 (2000).
8 Goldstein, R. M., Zebker, H. A. & Werner, C. L. Satellite radar interferometry two-dimensional phase unwrapping. *Radio Sci.* **23**, 713-720 (1988).
9 Chen, C. W. & Zebker, H. A. Phase unwrapping for large SAR interferograms: Statistical segmentation and generalized network models. *IEEE Transactions on Geoscience and Remote Sensing* **40**, 1709-1719, doi:Doi 10.1109/Tgrs.2002.802453 (2002).
10 Lohman, R. B. & Simons, M. Some thoughts on the use of InSAR data to constrain models of surface deformation: Noise structure and data downsampling. *Geochemistry Geophysics Geosystems* **6**, -, doi:Doi 10.1029/2004gc000841 (2005).
11 Pathier, E. *et al.* Displacement field and slip distribution of the 2005 Kashmir earthquake from SAR imagery. *Geophys. Res. Lett.* **33**, -, doi:Doi 10.1029/2006gl027193 (2006).
12 Ji, C., Wald, D. J. & Helmberger, D. V. Source description of the 1999 Hector Mine, California, earthquake, part I: Wavelet domain inversion theory and resolution analysis. *Bull. Seismol. Soc. Am.* **92**, 1192-1207 (2002).
13 Ji, C., Wald, D. J. & Helmberger, D. V. Source description of the 1999 Hector Mine, California, earthquake, part II: Complexity of slip history. *Bull. Seismol. Soc. Am.* **92**, 1208-1226 (2002).
14 Rothman, D. H. Automatic Estimation of Large Residual Statics Corrections. *Geophysics* **51**, 332-346 (1986).
15 Sen, M. K. & Stoffa, P. L. Nonlinear One-Dimensional Seismic Wave-Form Inversion Using Simulated Annealing. *Geophysics* **56**, 1624-1638 (1991).
16 Fletcher, J. M. & Spelz, R. M. Patterns of Quaternary deformation and rupture propagation associated with an active low-angle normal fault, Laguna Salada, Mexico: Evidence of a rolling hinge? *Geosphere* **5**, 385-407 (2009).
17 Hartzell, S. & Helmberger, D. V. Strong-Motion Modeling of the Imperial-Valley Earthquake of 1979. *Bull. Seismol. Soc. Am.* **72**, 571-596 (1982).

SCSN/CISN Recorded Seismicity (red) April 4– May 25, 2010

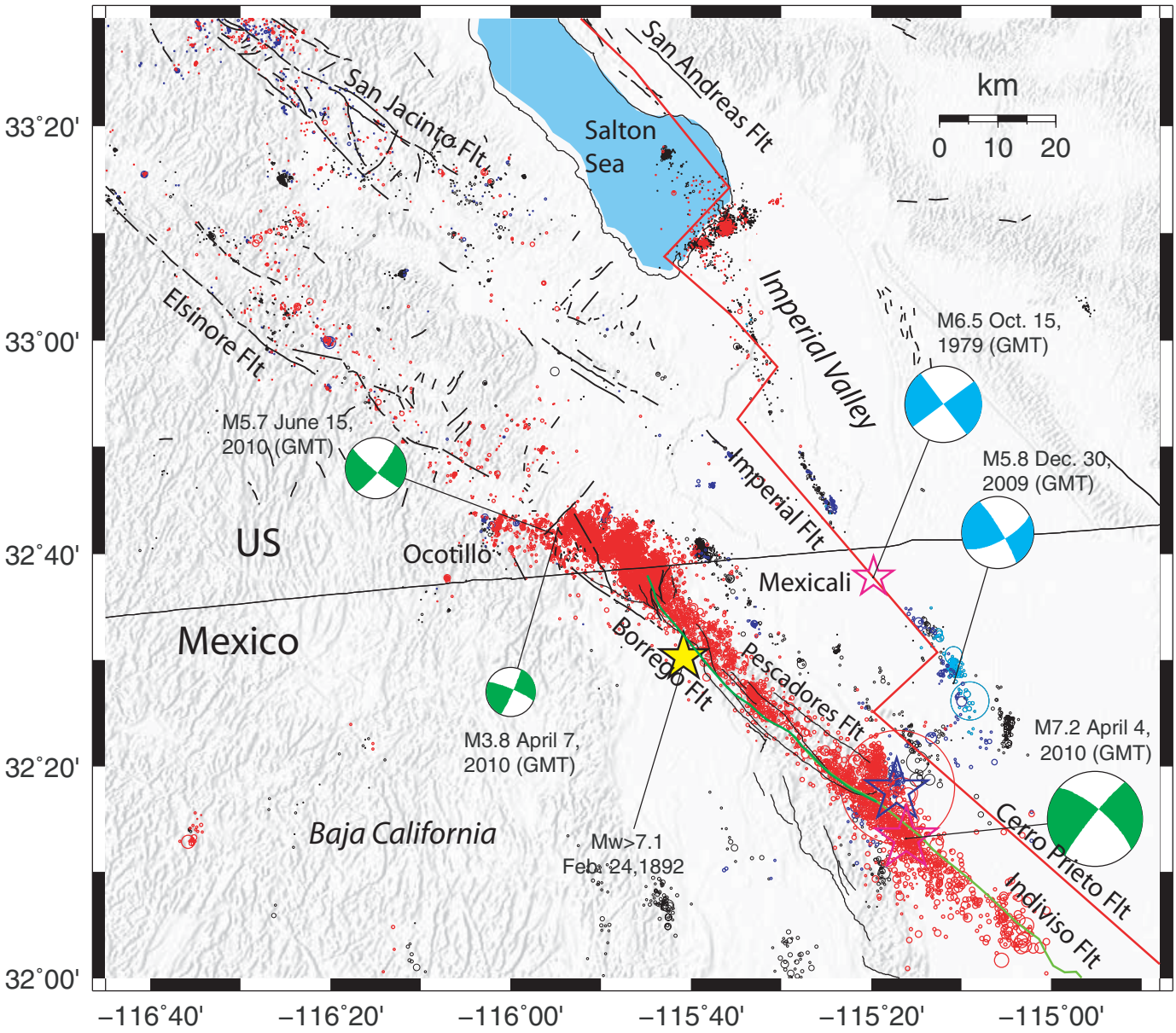

Figure S1

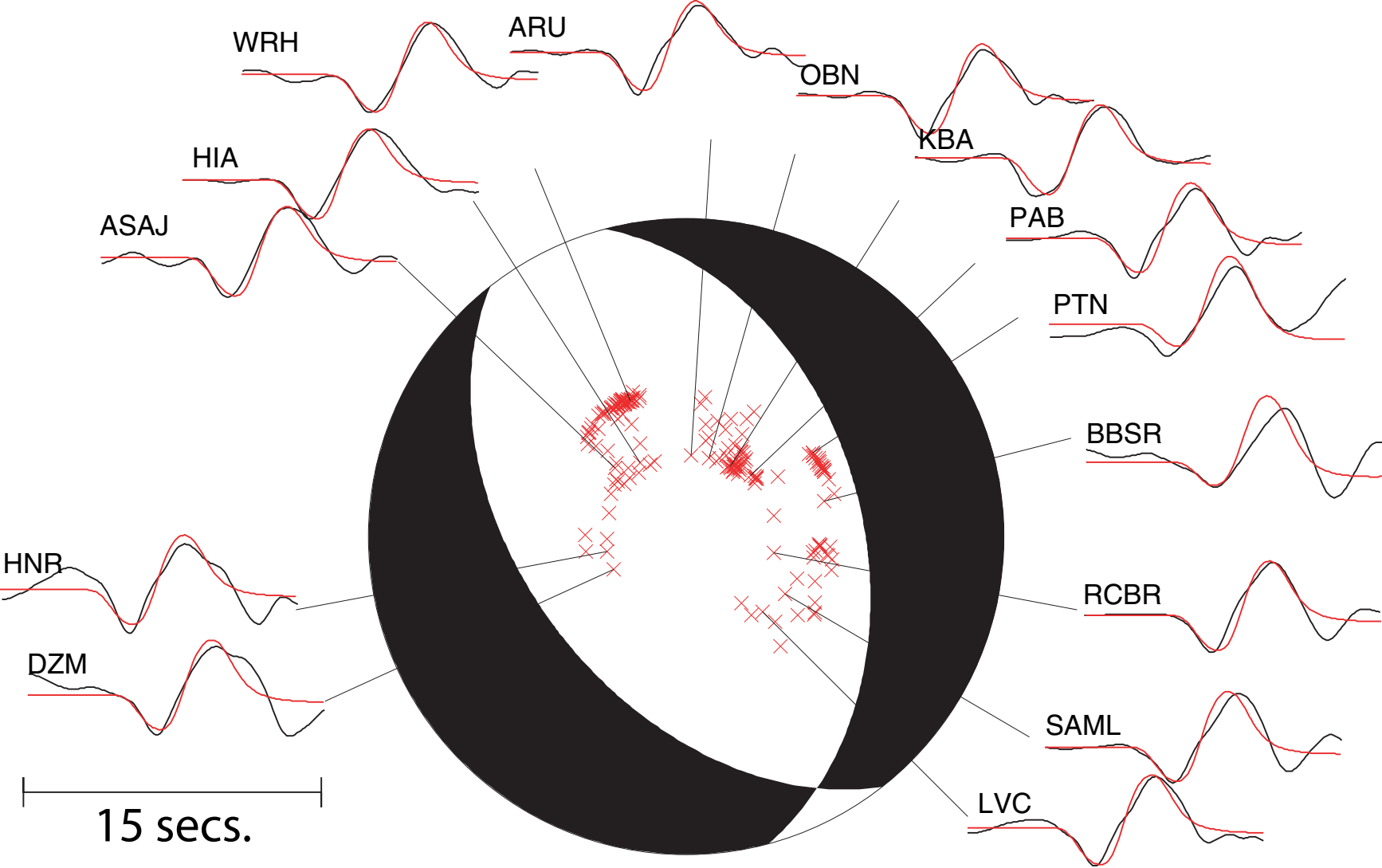
WRH
ARU
OBN
KBA
HIA
ASAJ
PAB
PTN
BBSR
HNR
RCBR
DZM
SAML
LVC
15 secs.

Figure S2

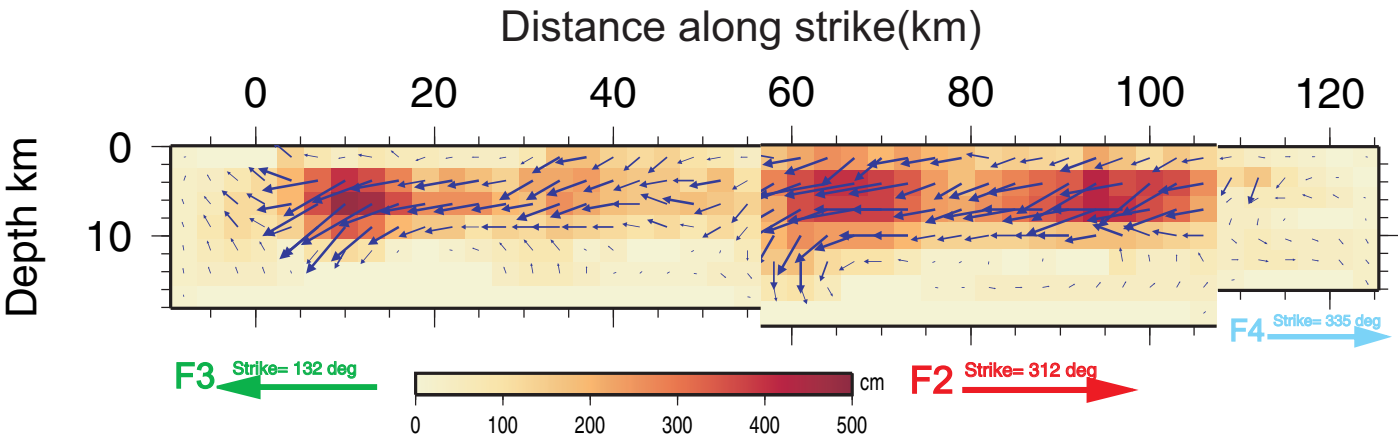
Distance along strike(km)
0
20
40
60
80
100
120
Depth km
0
10
F3
Strike= 132 deg
cm
0
100
200
300
400
500
F2
Strike= 312 deg
F4
Strike= 335 deg

Figure S3

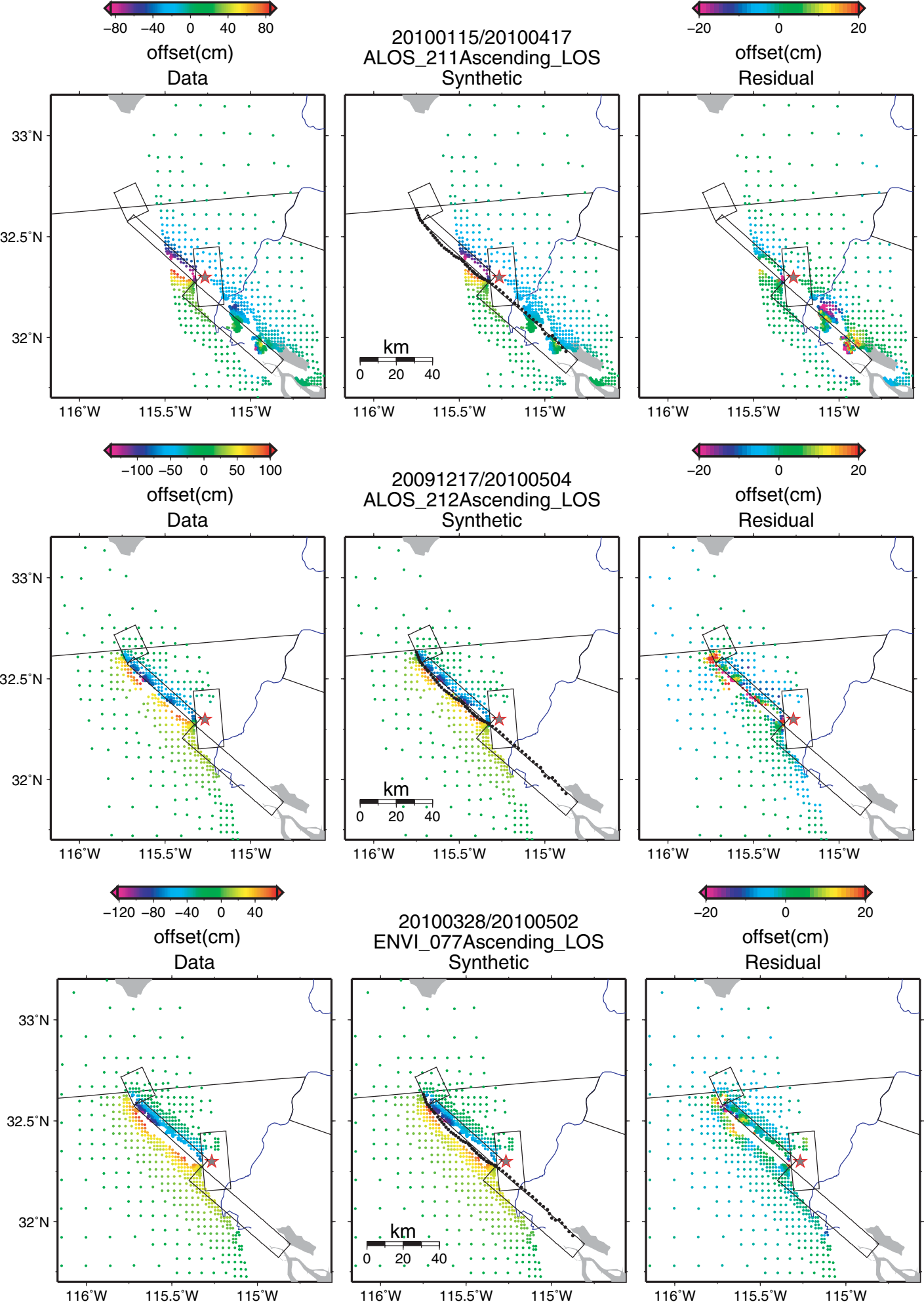
−80 −40 0 40 80
offset(cm)
Data
20100115/20100417
ALOS_211Ascending_LOS
Synthetic
−20 0 20
offset(cm)
Residual
33°N
32.5°N
32°N
116°W
115.5°W
115°W
km
0 20 40
−100 −50 0 50 100
offset(cm)
Data
20091217/20100504
ALOS_212Ascending_LOS
Synthetic
−20 0 20
offset(cm)
Residual
−120 −80 −40 0 40
offset(cm)
Data
20100328/20100502
ENVI_077Ascending_LOS
Synthetic
−20 0 20
offset(cm)
Residual

Figure S4

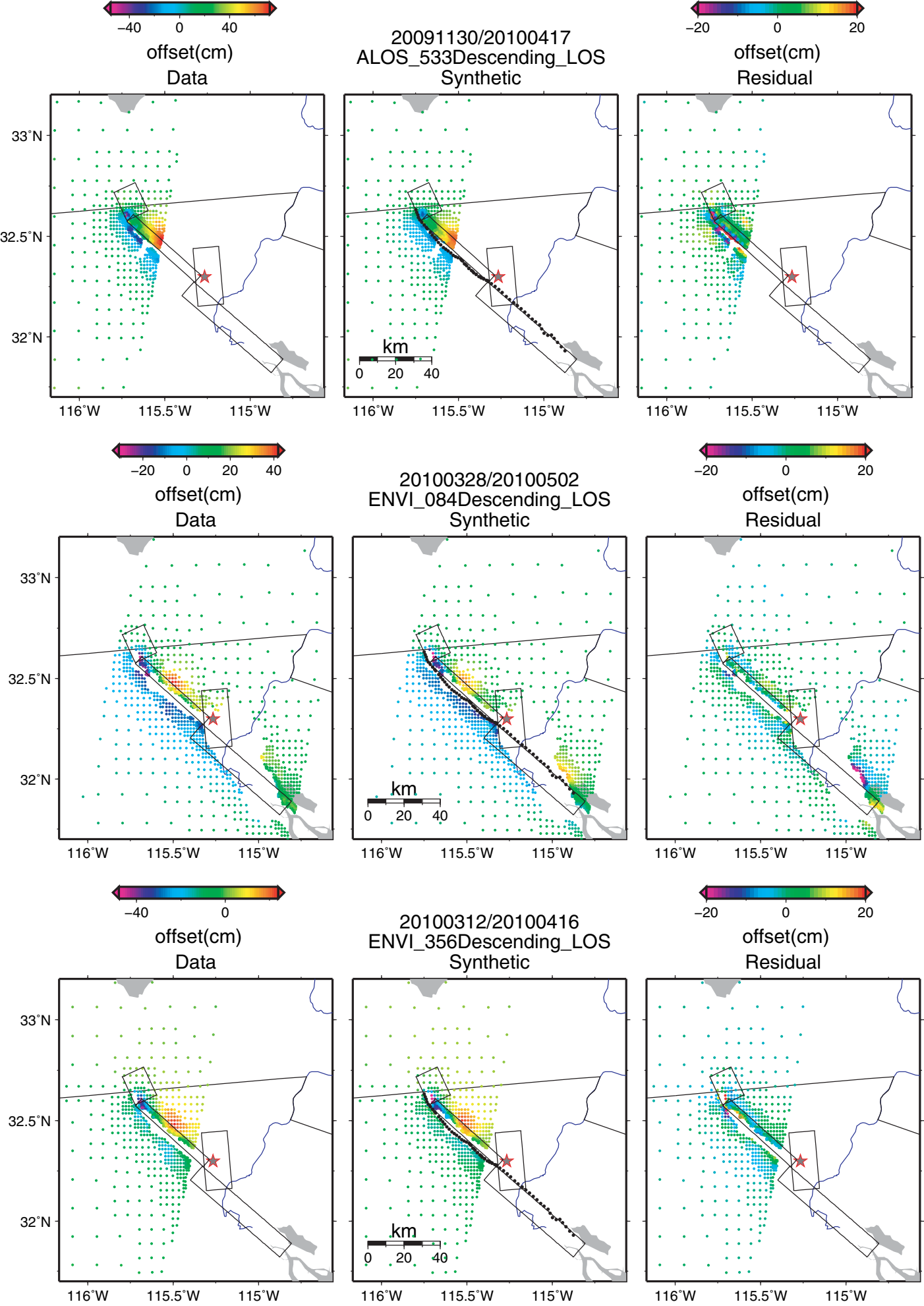
−40 0 40
offset(cm)
Data
20091130/20100417
ALOS_533Descending_LOS
Synthetic
−20 0 20
offset(cm)
Residual
33°N
32.5°N
32°N
km
0 20 40
116°W 115.5°W 115°W
−20 0 20 40
offset(cm)
Data
20100328/20100502
ENVI_084Descending_LOS
Synthetic
−20 0 20
offset(cm)
Residual
−40 0
offset(cm)
Data
20100312/20100416
ENVI_356Descending_LOS
Synthetic
−20 0 20
offset(cm)
Residual

Figure S5

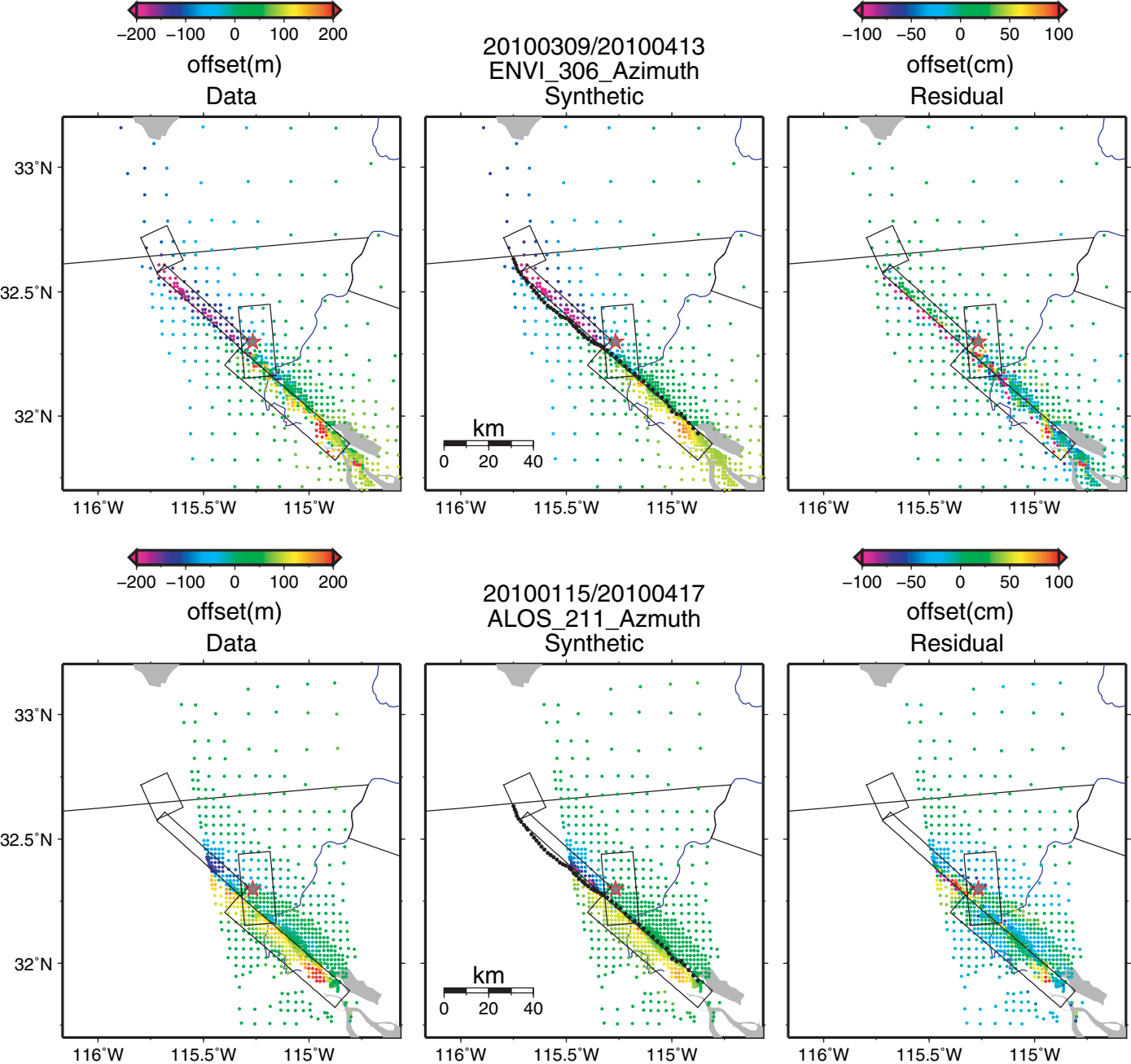
−200 −100 0 100 200
offset(m)
Data
20100309/20100413
ENVI_306_Azimuth
Synthetic
−100 −50 0 50 100
offset(cm)
Residual
33°N
32.5°N
32°N
km
0 20 40
116°W
115.5°W
115°W
−200 −100 0 100 200
offset(m)
Data
20100115/20100417
ALOS_211_Azmuth
Synthetic
−100 −50 0 50 100
offset(cm)
Residual
33°N
32.5°N
32°N
km
0 20 40
116°W
115.5°W
115°W

Figure S6

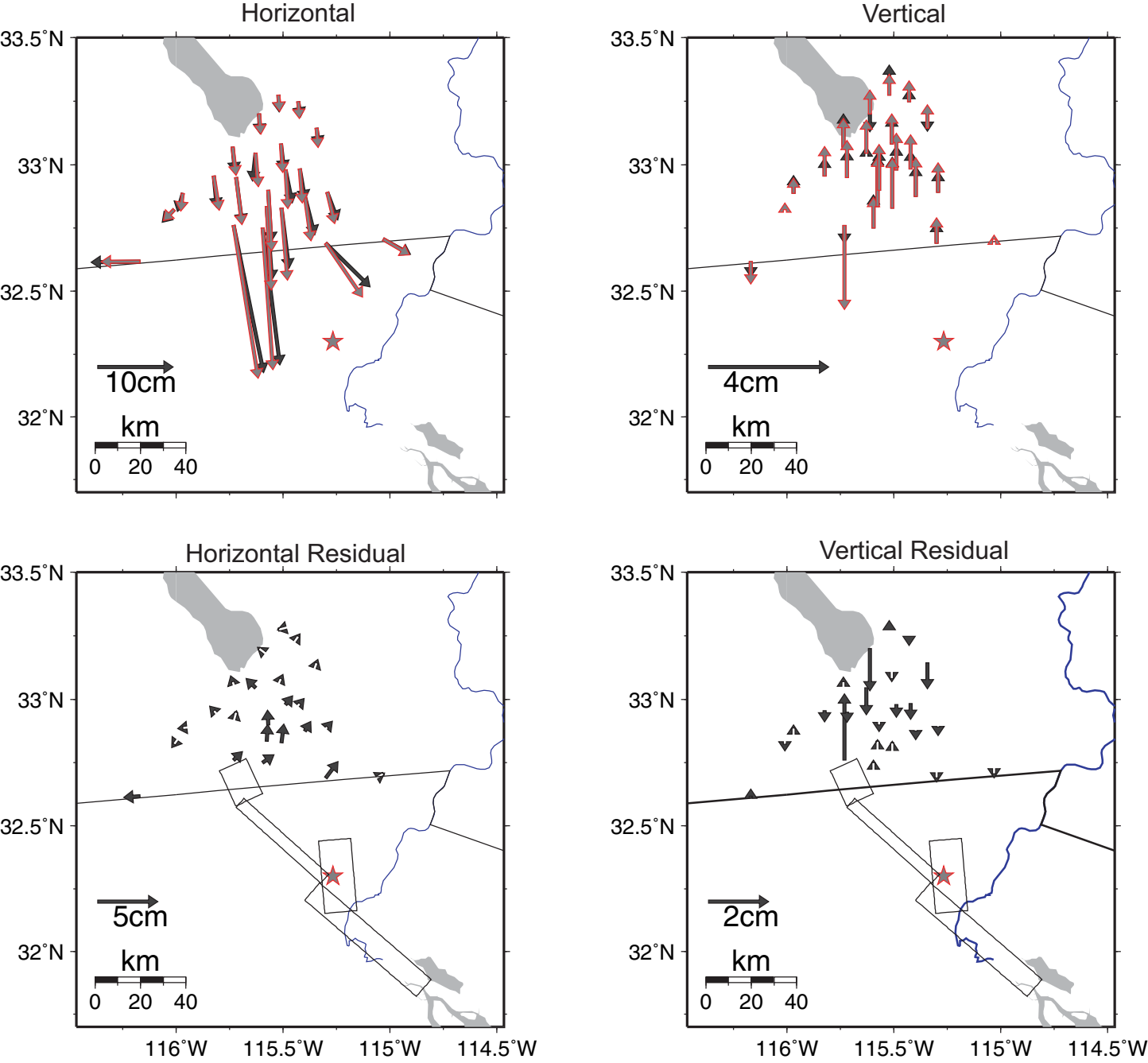
Horizontal
Vertical
Horizontal Residual
Vertical Residual
33.5°N
33°N
32.5°N
32°N
116°W
115.5°W
115°W
114.5°W
10cm
4cm
5cm
2cm
km
0 20 40

Figure S7

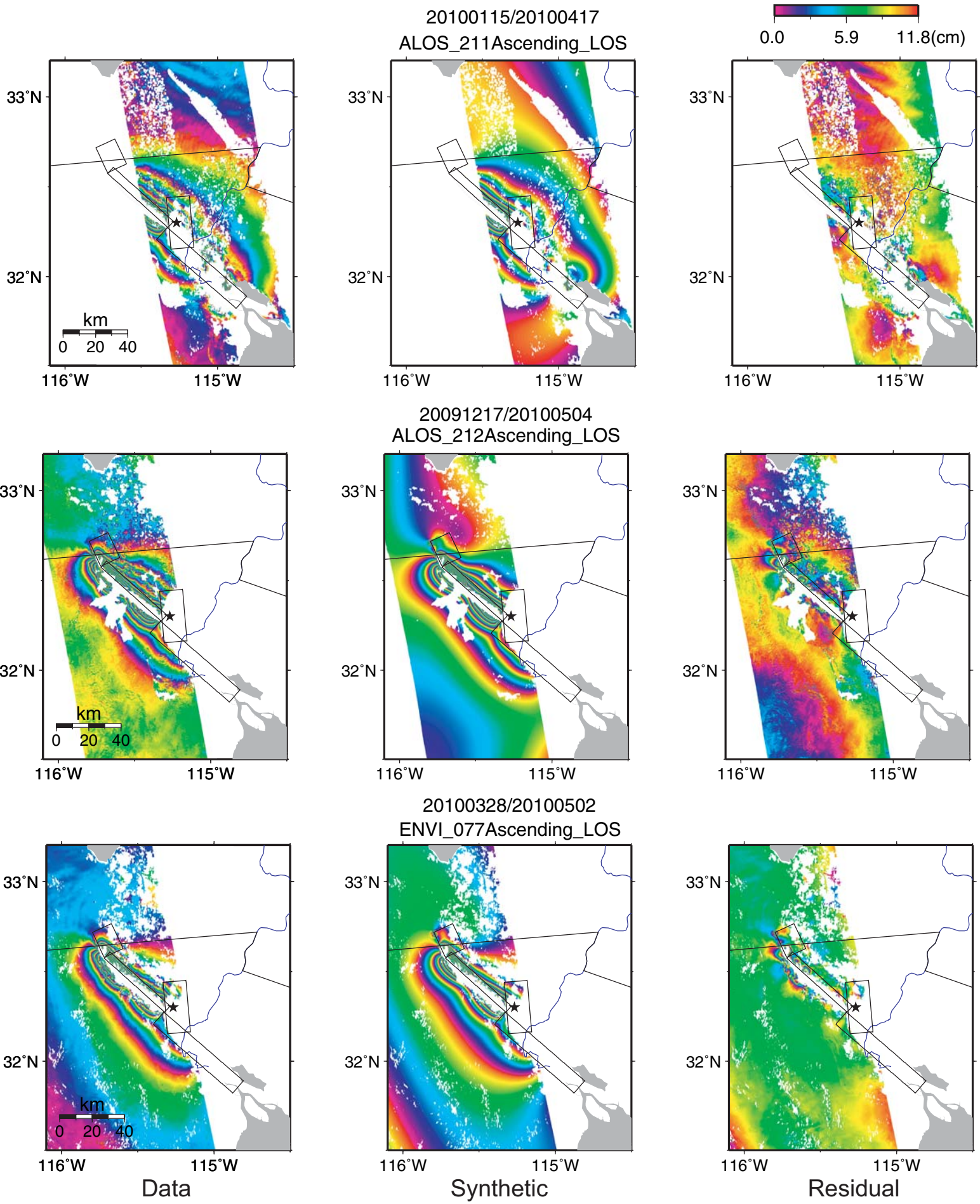
20100115/20100417
ALOS_211Ascending_LOS
0.0
5.9
11.8(cm)
20091217/20100504
ALOS_212Ascending_LOS
20100328/20100502
ENVI_077Ascending_LOS
33°N
32°N
116°W
115°W
km
0 20 40
Data
Synthetic
Residual

Figure S8

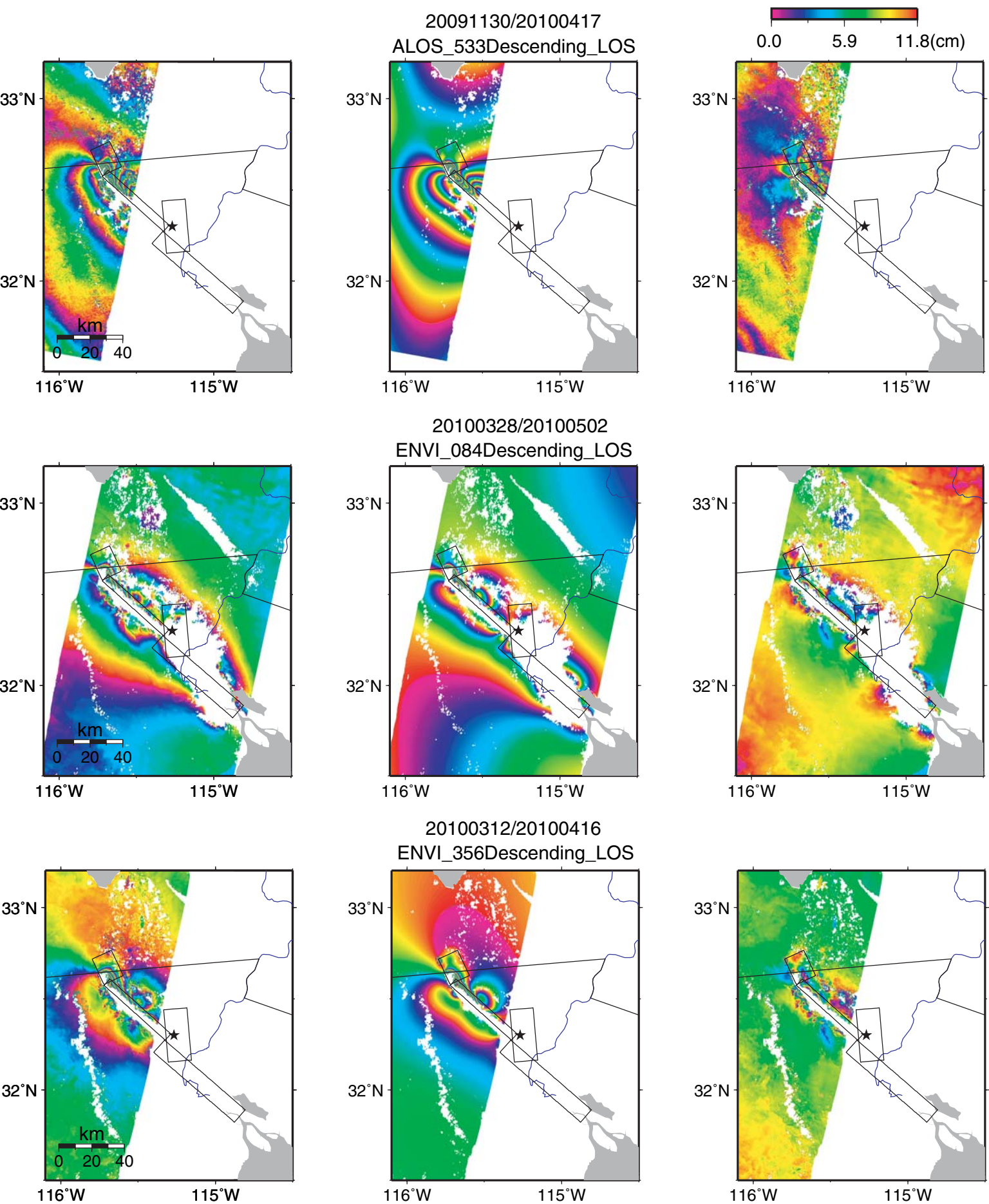
20091130/20100417
ALOS_533Descending_LOS
0.0
5.9
11.8(cm)
20100328/20100502
ENVI_084Descending_LOS
20100312/20100416
ENVI_356Descending_LOS
33°N
32°N
116°W
115°W
km
0 20 40
Data
Synthetic
Residual

Figure S9

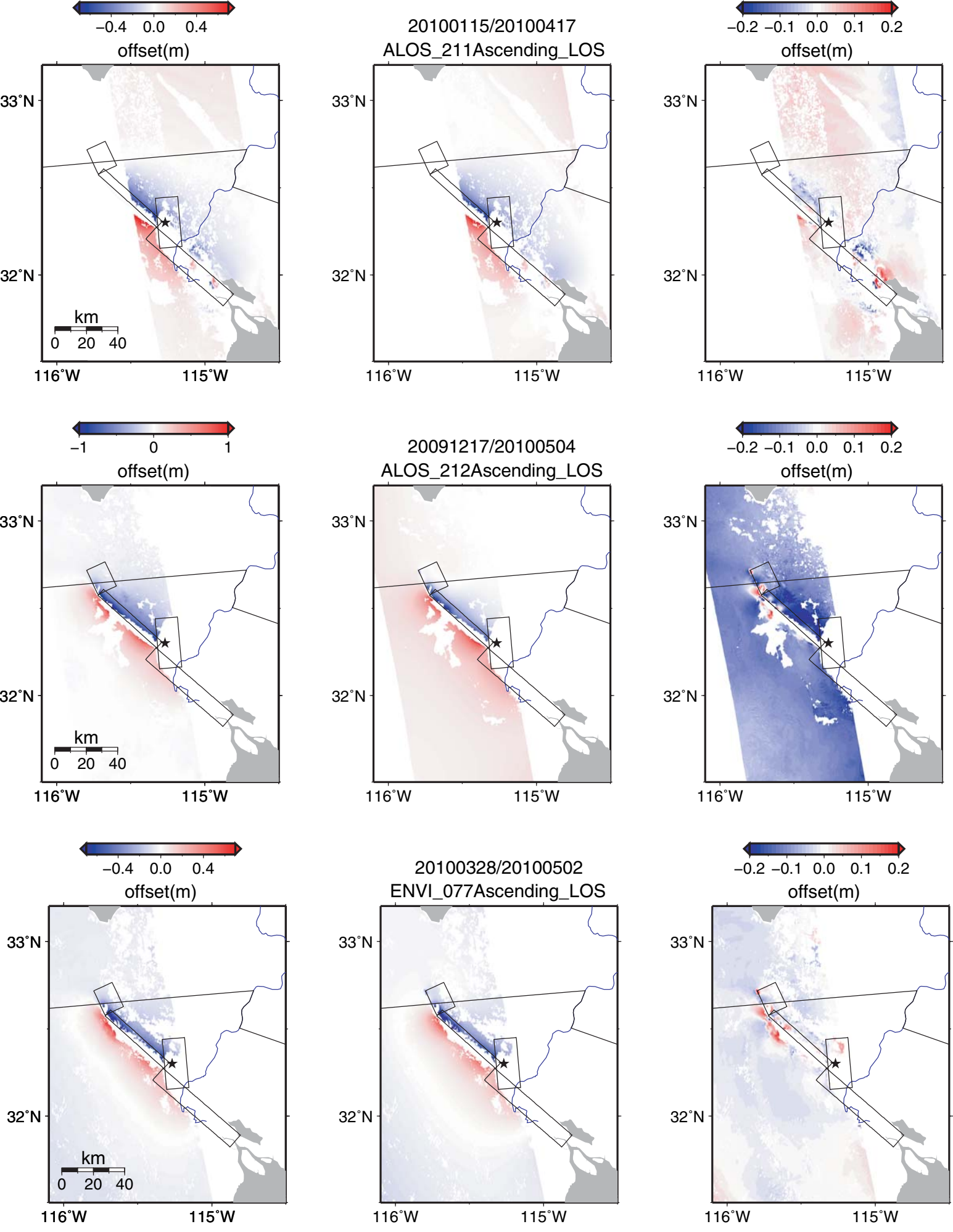
−0.4 0.0 0.4
offset(m)
20100115/20100417
ALOS_211Ascending_LOS
−0.2 −0.1 0.0 0.1 0.2
offset(m)
33°N
32°N
km
0 20 40
116°W
115°W
−1 0 1
offset(m)
20091217/20100504
ALOS_212Ascending_LOS
−0.2 −0.1 0.0 0.1 0.2
offset(m)
−0.4 0.0 0.4
offset(m)
20100328/20100502
ENVI_077Ascending_LOS
−0.2 −0.1 0.0 0.1 0.2
offset(m)
Data
Synthetic
Residual

Figure S10

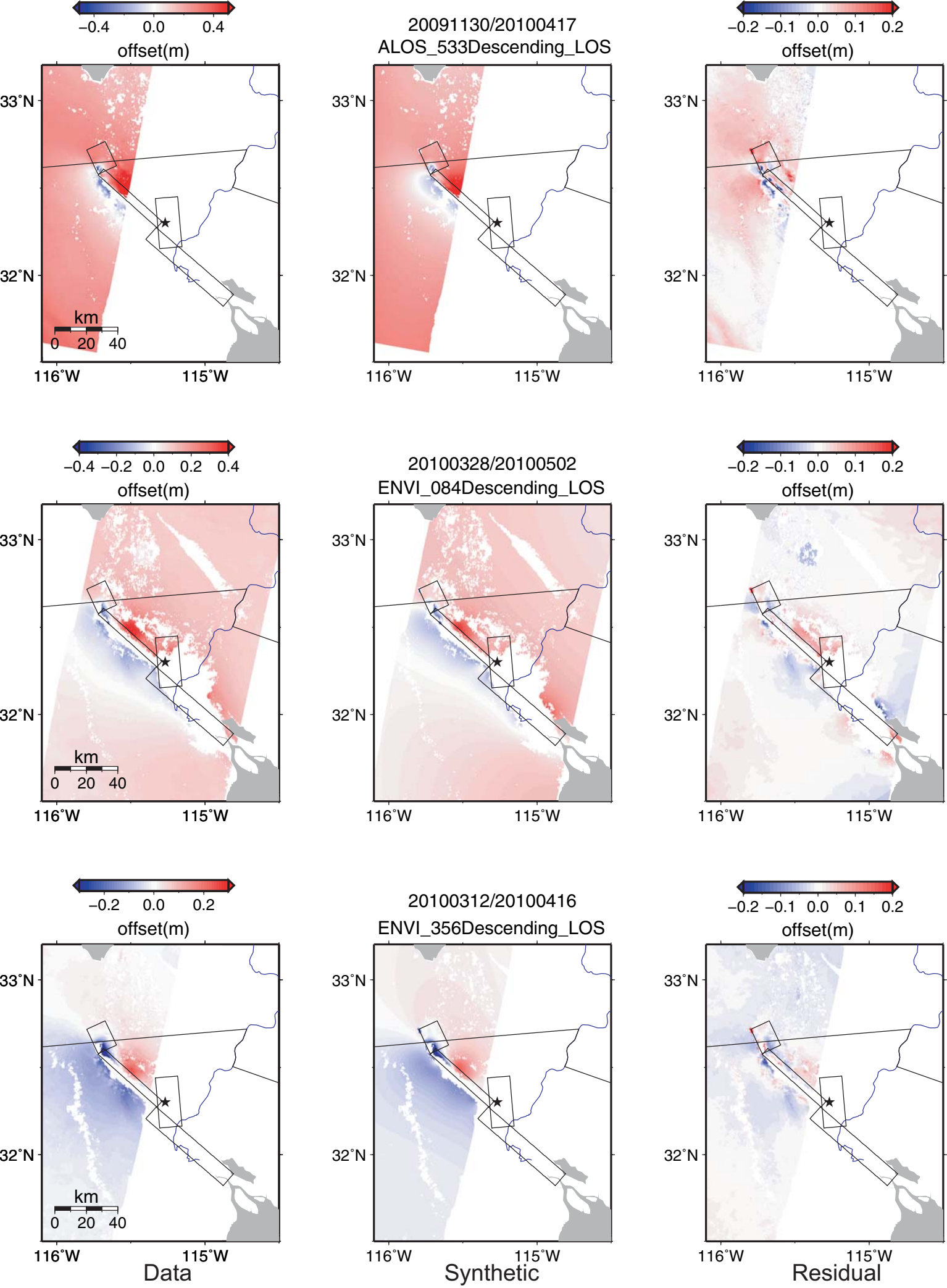
−0.4 0.0 0.4
offset(m)
20091130/20100417
ALOS_533Descending_LOS
−0.2 −0.1 0.0 0.1 0.2
offset(m)
33°N
32°N
km
0 20 40
116°W
115°W
−0.4 −0.2 0.0 0.2 0.4
offset(m)
20100328/20100502
ENVI_084Descending_LOS
−0.2 −0.1 0.0 0.1 0.2
offset(m)
−0.2 0.0 0.2
offset(m)
20100312/20100416
ENVI_356Descending_LOS
−0.2 −0.1 0.0 0.1 0.2
offset(m)
Data
Synthetic
Residual

Figure S11

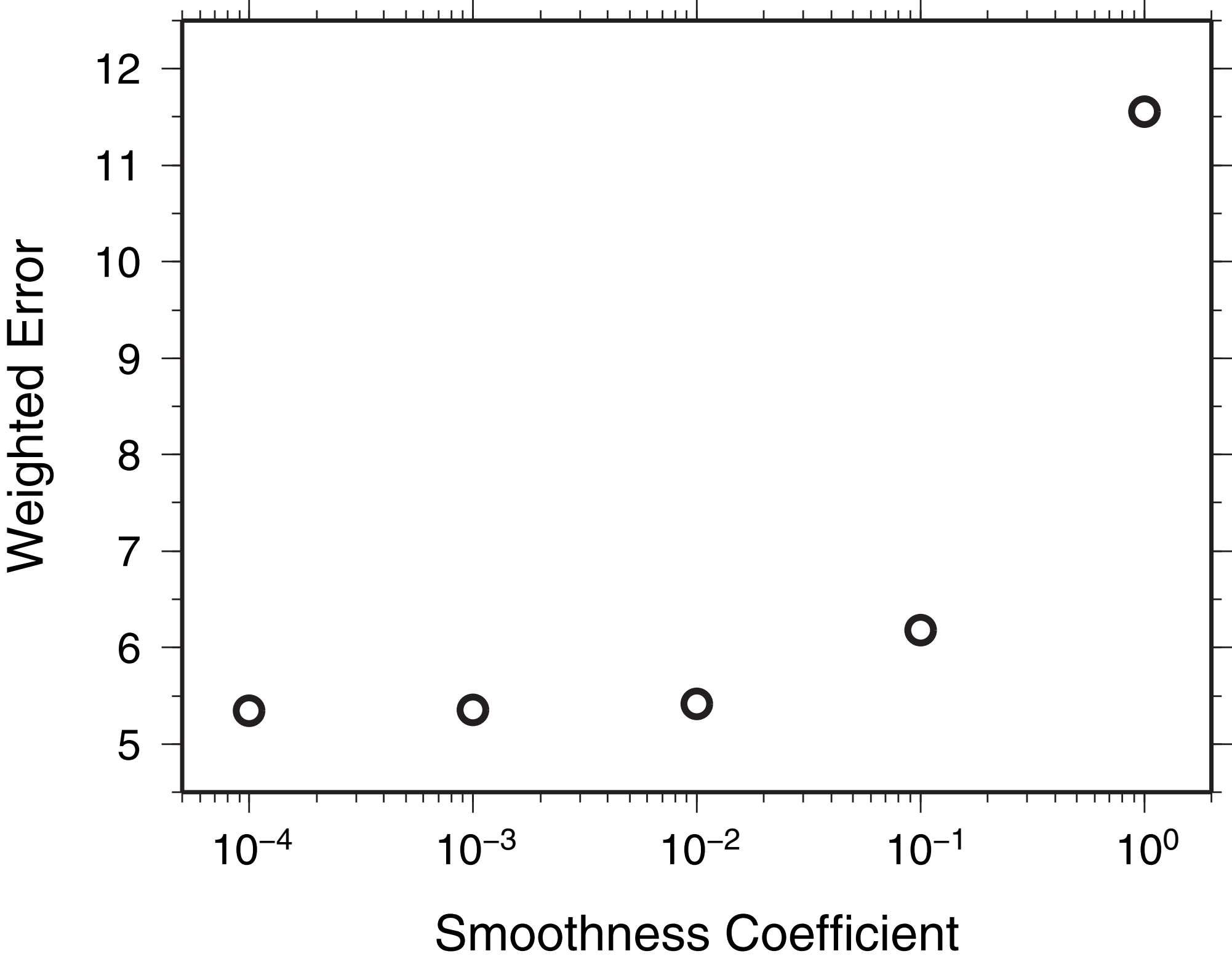
12
11
10
9
8
7
6
5
Weighted Error
10^{-4}
10^{-3}
10^{-2}
10^{-1}
10^{0}
Smoothness Coefficient

Figure S12

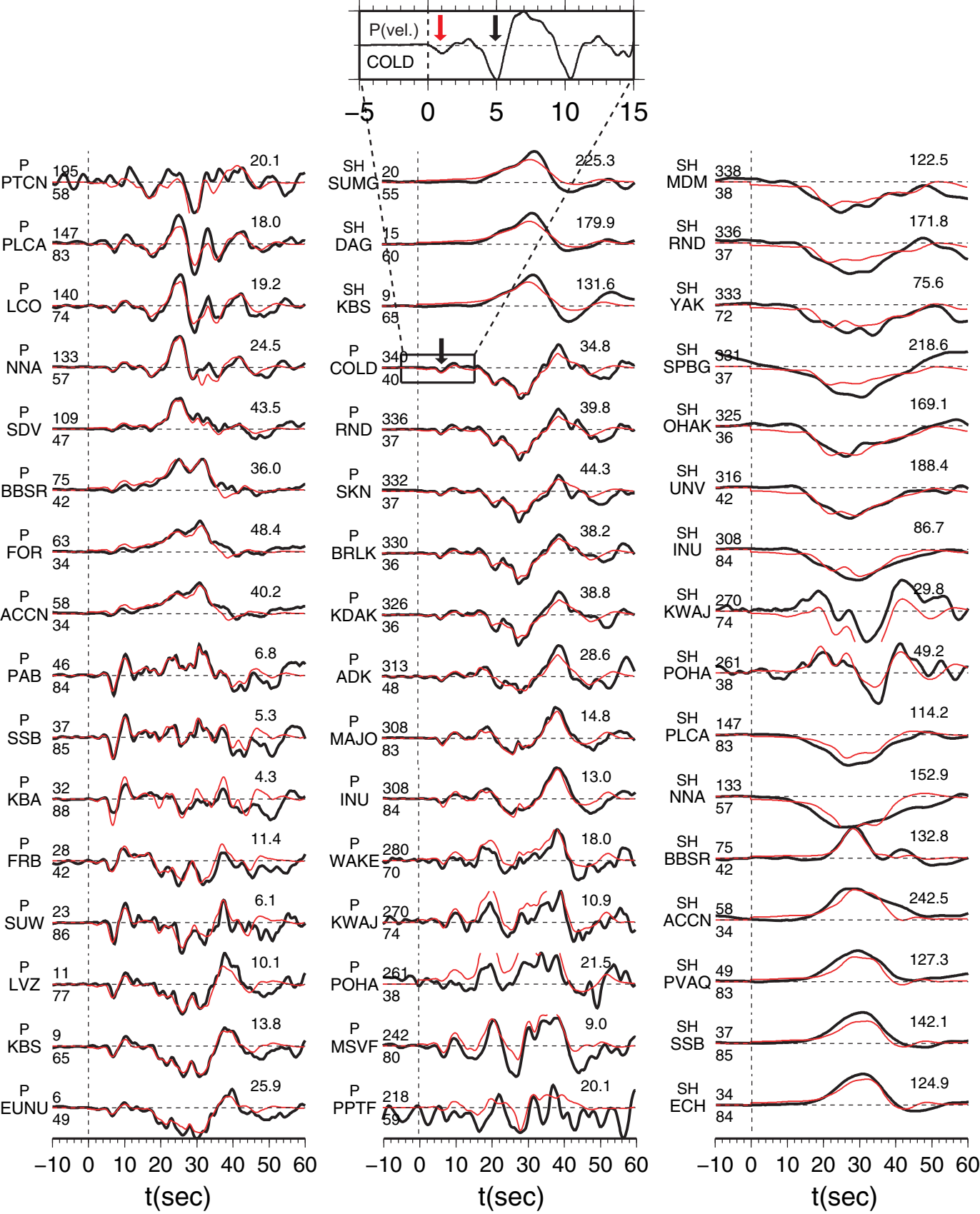
P(vel.)
COLD
−5 0 5 10 15
P PTCN 195 58 20.1
P PLCA 147 83 18.0
P LCO 140 74 19.2
P NNA 133 57 24.5
P SDV 109 47 43.5
P BBSR 75 42 36.0
P FOR 63 34 48.4
P ACCN 58 34 40.2
P PAB 46 84 6.8
P SSB 37 85 5.3
P KBA 32 88 4.3
P FRB 28 42 11.4
P SUW 23 86 6.1
P LVZ 11 77 10.1
P KBS 9 65 13.8
P EUNU 6 49 25.9
SH SUMG 20 55 225.3
SH DAG 15 60 179.9
SH KBS 9 65 131.6
P COLD 340 40 34.8
P RND 336 37 39.8
P SKN 332 37 44.3
P BRLK 330 36 38.2
P KDAK 326 36 38.8
P ADK 313 48 28.6
P MAJO 308 83 14.8
P INU 308 84 13.0
P WAKE 280 70 18.0
P KWAJ 270 74 10.9
P POHA 261 38 21.5
P MSVF 242 80 9.0
P PPTF 218 59 20.1
SH MDM 338 38 122.5
SH RND 336 37 171.8
SH YAK 333 72 75.6
SH SPBG 331 37 218.6
SH OHAK 325 36 169.1
SH UNV 316 42 188.4
SH INU 308 84 86.7
SH KWAJ 270 74 29.8
SH POHA 261 38 49.2
SH PLCA 147 83 114.2
SH NNA 133 57 152.9
SH BBSR 75 42 132.8
SH ACCN 58 34 242.5
SH PVAQ 49 83 127.3
SH SSB 37 85 142.1
SH ECH 34 84 124.9
−10 0 10 20 30 40 50 60
t(sec)
−10 0 10 20 30 40 50 60
t(sec)
−10 0 10 20 30 40 50 60
t(sec)

Figure S13

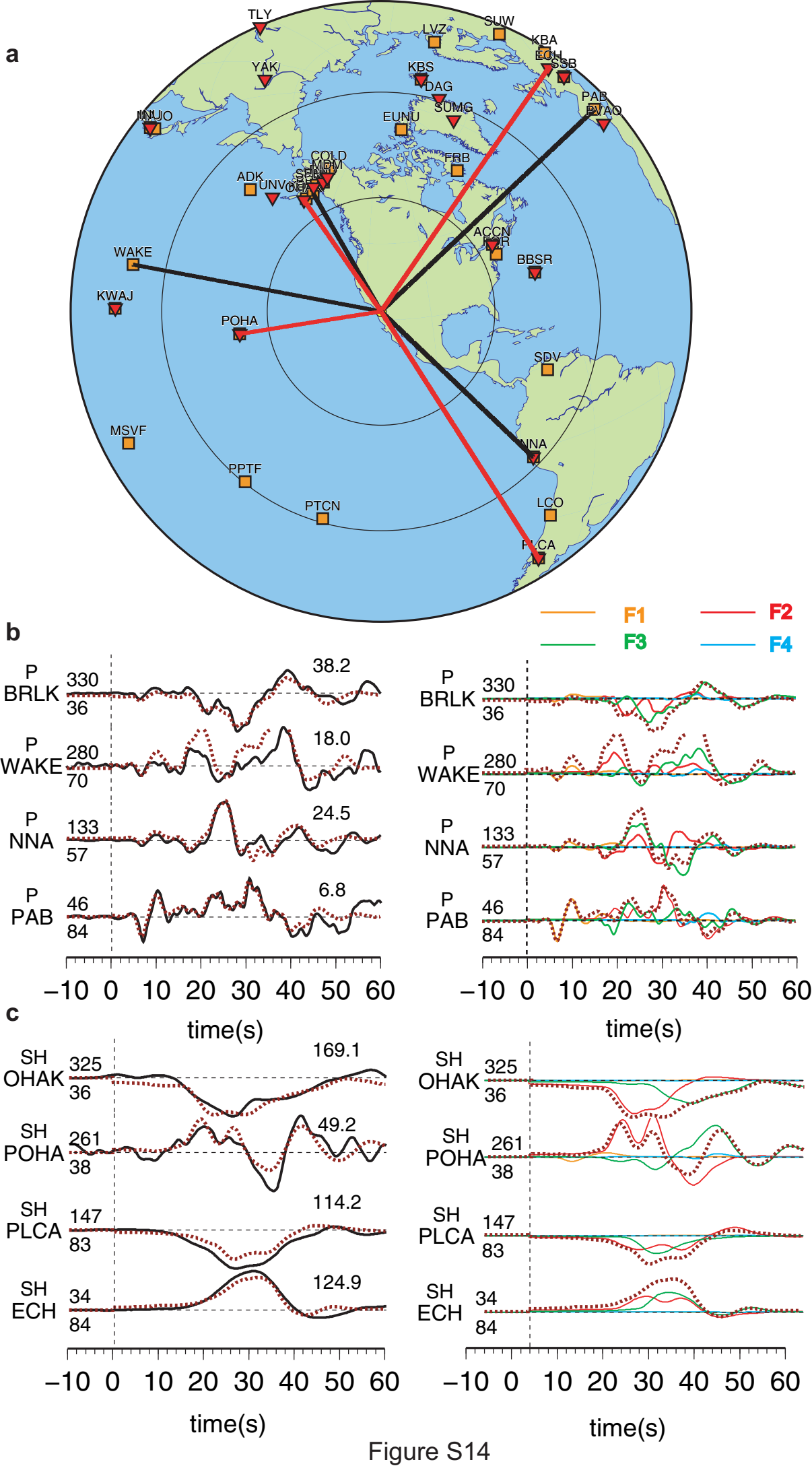
a
TLY
LVZ
SUW
KBA
ECH
SSB
YAK
KBS
DAG
SUMG
PAB
PVAQ
INUO
EUNU
FRB
COLD
ADK
UNV
WAKE
ACCN
BBSR
KWAJ
POHA
SDV
MSVF
NNA
PPTF
PTCN
LCO
PLCA
b
F1
F2
F3
F4
P BRLK 330 36
P WAKE 280 70
P NNA 133 57
P PAB 46 84
38.2
18.0
24.5
6.8
−10 0 10 20 30 40 50 60
time(s)
c
SH OHAK 325 36
SH POHA 261 38
SH PLCA 147 83
SH ECH 34 84
169.1
49.2
114.2
124.9
−10 0 10 20 30 40 50 60
time(s)

Figure S14

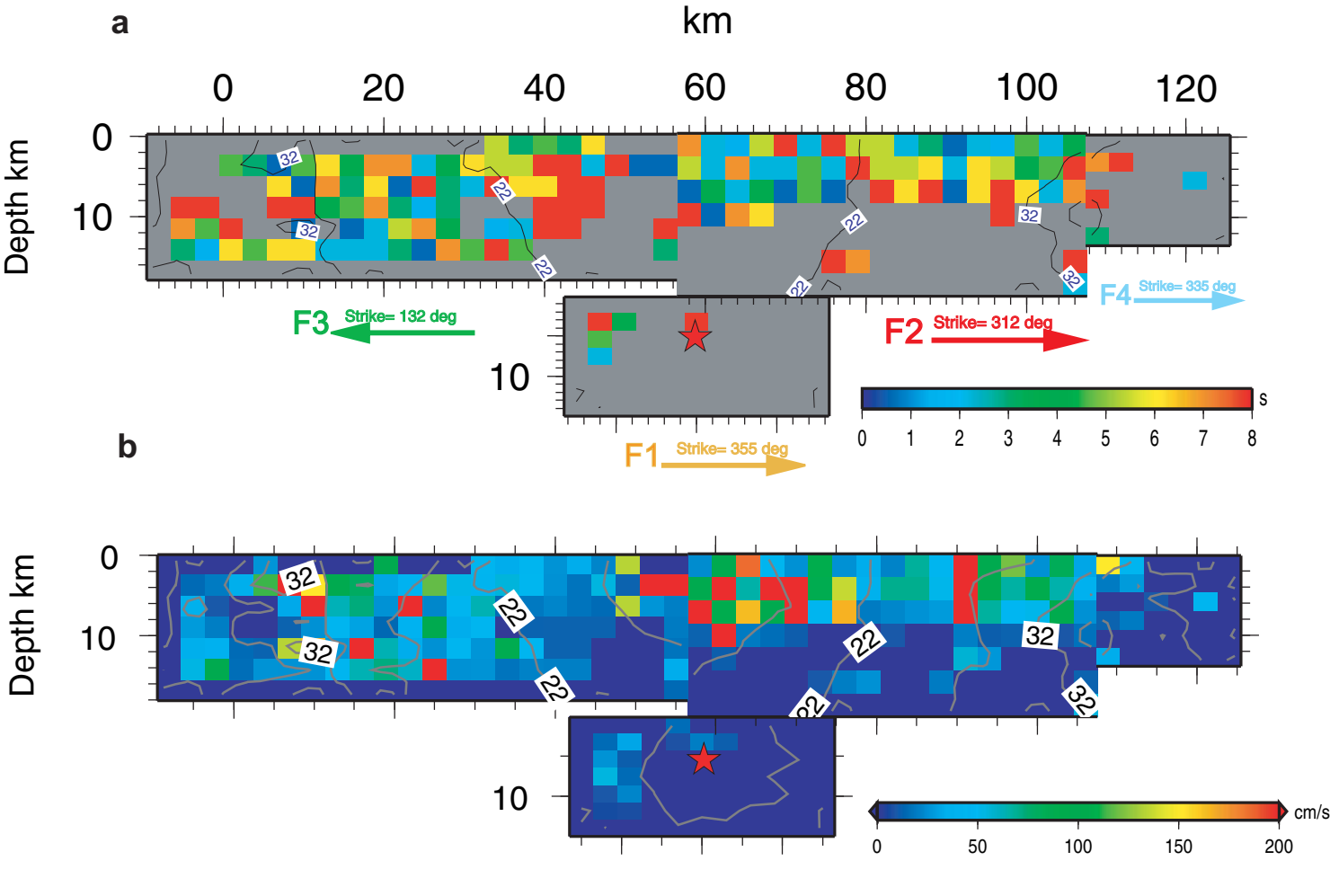
a
km
0
20
40
60
80
100
120
Depth km
0
10
32
22
F3
Strike= 132 deg
F2
Strike= 312 deg
F4
Strike= 335 deg
F1
Strike= 355 deg
s
0
1
2
3
4
5
6
7
8
b
cm/s
0
50
100
150
200

Figure S15

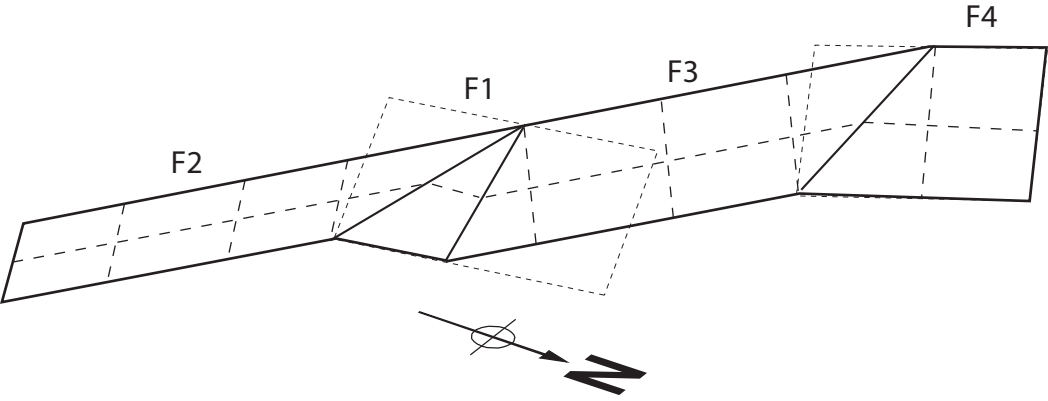

Figure S16

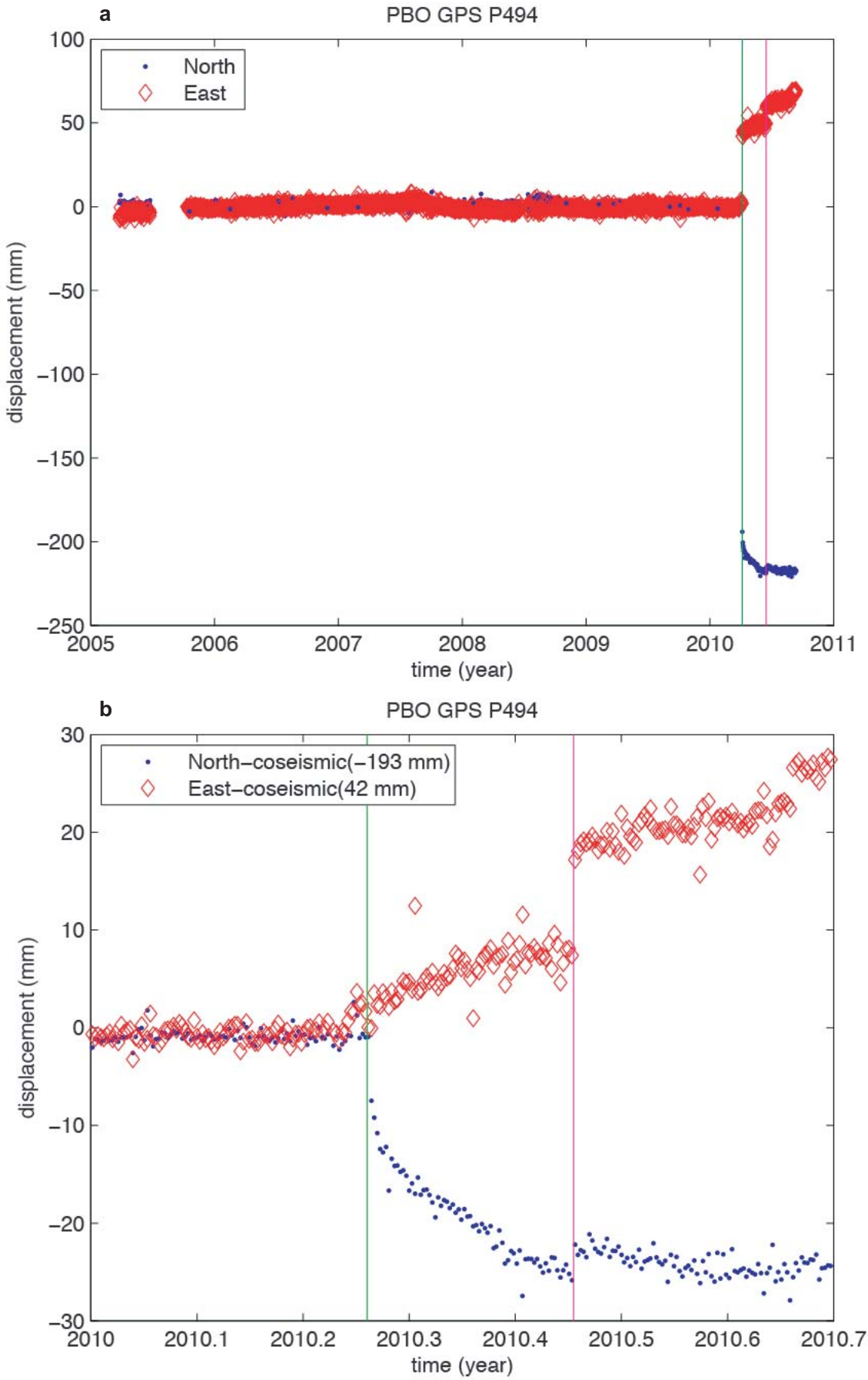
a
PBO GPS P494
North
East
displacement (mm)
time (year)
b
PBO GPS P494
North–coseismic(–193 mm)
East–coseismic(42 mm)
displacement (mm)
time (year)

Figure S17

Fault_segment = 1 nx(along strike)= 11 Dx= 3.00km ny(down dip)= 7 Dy = 3.00km

Lon.(°)	Lat.(°)	Depth(km)	Slip(cm)	Rupture start time	Rise time	Rake(°)	Strike(°)	Dip(°)
-115.305	32.153	1.21	0	8.08	7.8	-120	355	45
-115.307	32.18	1.21	0	7.06	3.8	-120	355	45
-115.31	32.206	1.21	30	7.21	2.2	-76	355	45
-115.313	32.233	1.21	30	4.99	1.4	-60	355	45
-115.316	32.26	1.21	60	3.95	4.6	-60	355	45
-115.319	32.287	1.21	0	2.4	4.6	-120	355	45
-115.321	32.314	1.21	0	2.68	6.2	-120	355	45
-115.324	32.341	1.21	0	3.54	7.8	-120	355	45
-115.327	32.368	1.21	0	5.41	7.8	-120	355	45
-115.33	32.395	1.21	0	6.39	4.6	-120	355	45
-115.332	32.422	1.21	0	6.73	5.4	-120	355	45
-115.282	32.154	3.33	10	9	4.6	-120	355	45
-115.285	32.181	3.33	120	7.28	8.6	-120	355	45
-115.288	32.208	3.33	120	5.93	4.6	-66	355	45
-115.291	32.235	3.33	40	4.47	7.8	-60	355	45
-115.293	32.262	3.33	60	2.5	7.8	-76	355	45
-115.296	32.289	3.33	160	2	8.6	-80	355	45
-115.299	32.316	3.33	90	2.83	8.6	-74	355	45
-115.302	32.343	3.33	0	2.68	4.6	-120	355	45
-115.304	32.37	3.33	0	4.99	3.8	-120	355	45
-115.307	32.396	3.33	0	8.25	5.4	-120	355	45
-115.31	32.423	3.33	5	8.5	7	-120	355	45
-115.26	32.156	5.45	10	8.82	4.6	-120	355	45
-115.262	32.183	5.45	120	7.5	5.4	-108	355	45
-115.265	32.21	5.45	80	5	7.8	-70	355	45
-115.268	32.237	5.45	0	4	2.2	-120	355	45
-115.271	32.264	5.45	20	1.87	2.2	-120	355	45
-115.274	32.291	5.45	40	0	2.2	-120	355	45
-115.276	32.317	5.45	40	1.87	3	-120	355	45
-115.279	32.344	5.45	0	2.4	3	-120	355	45
-115.282	32.371	5.45	0	3.75	3	-120	355	45
-115.285	32.398	5.45	0	5.45	8.6	-120	355	45
-115.287	32.425	5.45	5	9.37	1.4	-120	355	45
-115.237	32.158	7.57	10	9	6.2	-120	355	45
-115.24	32.185	7.57	120	5.89	3	-120	355	45
-115.243	32.212	7.57	70	4.99	5.4	-120	355	45
-115.246	32.238	7.57	0	4.19	1.4	-120	355	45
-115.248	32.265	7.57	0	2.36	2.2	-120	355	45
-115.251	32.292	7.57	0	1.87	7.8	-120	355	45
-115.254	32.319	7.57	0	1.93	2.2	-120	355	45
-115.257	32.346	7.57	0	4.47	3.8	-120	355	45
-115.259	32.373	7.57	0	6.32	3.8	-120	355	45
-115.262	32.4	7.57	0	5.62	7.8	-120	355	45
-115.265	32.427	7.57	0	9	7	-120	355	45
-115.215	32.159	9.69	5	6.46	1.4	-120	355	45
-115.217	32.186	9.69	70	7.89	7.8	-120	355	45
-115.22	32.213	9.69	50	5.69	3	-120	355	45
-115.223	32.24	9.69	0	4.99	8.6	-120	355	45
-115.226	32.267	9.69	0	2.68	6.2	-120	355	45
-115.229	32.294	9.69	0	2.73	4.6	-120	355	45
-115.231	32.321	9.69	0	4.47	1.4	-120	355	45
-115.234	32.348	9.69	0	3.69	7.8	-120	355	45
-115.237	32.374	9.69	0	4.33	2.2	-120	355	45
-115.24	32.401	9.69	20	6.71	1.4	-120	355	45
-115.242	32.428	9.69	10	6.73	1.4	-120	355	45
-115.192	32.161	11.81	10	10.29	8.6	-120	355	45
-115.195	32.188	11.81	50	8.82	7.8	-120	355	45
-115.198	32.215	11.81	60	7.49	8.6	-120	355	45
-115.201	32.242	11.81	40	6.36	2.2	-62	355	45

-115.203	32.269	11.81	0	3.79	2.2	-120	355	45
-115.206	32.295	11.81	0	3.91	6.2	-120	355	45
-115.209	32.322	11.81	0	4.52	8.6	-120	355	45
-115.212	32.349	11.81	0	6.76	8.6	-120	355	45
-115.214	32.376	11.81	0	6.7	7.8	-120	355	45
-115.217	32.403	11.81	0	6.25	8.6	-120	355	45
-115.22	32.43	11.81	10	11.66	1.4	-120	355	45
-115.17	32.163	13.94	10	9.6	8.6	-120	355	45
-115.172	32.19	13.94	0	9.98	5.4	-120	355	45
-115.175	32.216	13.94	0	6.25	3	-120	355	45
-115.178	32.243	13.94	0	5.83	4.6	-120	355	45
-115.181	32.27	13.94	0	5.62	8.6	-120	355	45
-115.184	32.297	13.94	0	8	6.2	-120	355	45
-115.186	32.324	13.94	0	6.51	3	-120	355	45
-115.189	32.351	13.94	0	5.83	3.8	-120	355	45
-115.192	32.378	13.94	0	8.33	1.4	-120	355	45
-115.195	32.405	13.94	0	7.38	8.6	-120	355	45
-115.197	32.432	13.94	10	11.3	4.6	-120	355	45

Fault_segment = 2 nx(along strike)= 17 Dx= 3.00km ny(down dip)= 7 Dy= 3.00km

-115.324	32.273	1.53	170	13.26	7.8	-180	312	75
-115.348	32.291	1.53	220	14.4	3	-175.62	312	75
-115.372	32.309	1.53	260	15.98	2.2	-164.69	312	75
-115.395	32.327	1.53	245	17.45	6.2	-145	312	75
-115.419	32.345	1.53	200	18.47	8.6	-145	312	75
-115.443	32.363	1.53	235	19.38	3	-173.44	312	75
-115.467	32.381	1.53	200	21.05	8.6	-168.75	312	75
-115.49	32.399	1.53	181	22.34	6.2	-168.75	312	75
-115.514	32.417	1.53	120	23.64	6.2	-180	312	75
-115.538	32.435	1.53	150	24.93	3	-163.12	312	75
-115.561	32.453	1.53	130	25.2	3.8	-168.75	312	75
-115.585	32.471	1.53	120	24.86	1.4	-163.12	312	75
-115.609	32.49	1.53	220	25.93	3	-163.12	312	75
-115.633	32.508	1.53	170	27	2.2	-163.12	312	75
-115.656	32.526	1.53	118.5	28.07	5.4	-163.12	312	75
-115.68	32.544	1.53	180	30.75	3	-157.5	312	75
-115.704	32.562	1.53	120	30.21	4.6	-168.75	312	75
-115.319	32.278	4.43	520	13.62	6.2	160	312	75
-115.342	32.296	4.43	440	14.68	3	-156.25	312	75
-115.366	32.314	4.43	460	15.54	7.8	-168.75	312	75
-115.39	32.332	4.43	540	17.07	3	178.75	312	75
-115.414	32.35	4.43	440	17.98	3	-175	312	75
-115.437	32.368	4.43	400	20.29	5.4	-168.75	312	75
-115.461	32.386	4.43	300	19.92	3	-156.25	312	75
-115.485	32.404	4.43	280	22.43	8.6	-156.25	312	75
-115.508	32.422	4.43	380	23.71	6.2	-168.75	312	75
-115.532	32.441	4.43	380	23.78	6.2	-168.75	312	75
-115.556	32.459	4.43	320	25.58	7	-162.5	312	75
-115.58	32.477	4.43	560	26.81	3	-150	312	75
-115.603	32.495	4.43	600	29.78	7	-156.25	312	75
-115.627	32.513	4.43	360	31.14	6.2	-168.75	312	75
-115.651	32.531	4.43	400	28.83	4.6	-143.75	312	75
-115.675	32.549	4.43	300	30.79	5.4	-112.5	312	75
-115.698	32.567	4.43	300	35.22	8.6	-168.75	312	75
-115.313	32.283	7.33	280	14.4	1.4	-168.75	312	75
-115.337	32.301	7.33	400	15.39	4.6	-131.25	312	75
-115.361	32.319	7.33	360	16.04	3	-143.75	312	75
-115.384	32.337	7.33	360	17.37	4.6	178.75	312	75
-115.408	32.355	7.33	300	17.77	1.4	178.75	312	75
-115.432	32.373	7.33	200	20.62	5.4	-175	312	75
-115.455	32.392	7.33	100	21.93	1.4	160	312	75
-115.479	32.41	7.33	60	23.24	3.8	160	312	75
-115.503	32.428	7.33	180	23.92	8.6	-131.25	312	75

-115.527	32.446	7.33	160	24.24	7	-168.75	312	75
-115.55	32.464	7.33	220	27.25	8.6	160	312	75
-115.574	32.482	7.33	360	26.26	1.4	178.75	312	75
-115.598	32.5	7.33	420	29.94	7	178.75	312	75
-115.622	32.518	7.33	380	30.77	8.6	166.25	312	75
-115.645	32.536	7.33	320	32.09	7	160	312	75
-115.669	32.554	7.33	200	33.4	3	160	312	75
-115.693	32.572	7.33	180	34.72	7.8	160	312	75
-115.308	32.288	10.23	100	16.09	8.6	-118.75	312	75
-115.331	32.306	10.23	260	16.79	1.4	-100	312	75
-115.355	32.325	10.23	140	17.63	7.8	-100	312	75
-115.379	32.343	10.23	100	18.47	7	-100	312	75
-115.402	32.361	10.23	60	19.35	6.2	-100	312	75
-115.426	32.379	10.23	0	21.15	3.8	160	312	75
-115.45	32.397	10.23	0	20.34	4.6	160	312	75
-115.474	32.415	10.23	0	22.5	7.8	160	312	75
-115.497	32.433	10.23	80	24.27	8.6	-100	312	75
-115.521	32.451	10.23	0	24.23	2.2	160	312	75
-115.545	32.469	10.23	0	26.37	6.2	160	312	75
-115.569	32.487	10.23	80	25.25	4.6	-100	312	75
-115.592	32.505	10.23	80	29.25	7.8	-100	312	75
-115.616	32.523	10.23	100	31.52	8.6	160	312	75
-115.64	32.541	10.23	80	32.31	8.6	160	312	75
-115.663	32.559	10.23	60	34.2	7	160	312	75
-115.687	32.577	10.23	80	30.9	5.4	-100	312	75
-115.302	32.294	13.12	40	17.2	2.2	160	312	75
-115.326	32.312	13.12	80	17.64	7.8	-100	312	75
-115.35	32.33	13.12	0	17.86	1.4	160	312	75
-115.373	32.348	13.12	40	19.13	3	-100	312	75
-115.397	32.366	13.12	20	18.86	4.6	-100	312	75
-115.421	32.384	13.12	0	21.09	1.4	160	312	75
-115.444	32.402	13.12	0	22.7	7.8	160	312	75
-115.468	32.42	13.12	0	24.2	3	160	312	75
-115.492	32.438	13.12	0	25.43	4.6	160	312	75
-115.516	32.456	13.12	0	25.58	1.4	160	312	75
-115.539	32.474	13.12	40	26.39	7	-100	312	75
-115.563	32.492	13.12	80	27.18	2.2	-100	312	75
-115.587	32.51	13.12	60	26.89	3	-100	312	75
-115.611	32.528	13.12	0	31.33	2.2	160	312	75
-115.634	32.547	13.12	0	30.63	7	160	312	75
-115.658	32.565	13.12	0	31.79	5.4	160	312	75
-115.682	32.583	13.12	40	35.18	4.6	160	312	75
-115.297	32.299	16.02	0	18.12	7	160	312	75
-115.32	32.317	16.02	0	19.15	7.8	160	312	75
-115.344	32.335	16.02	0	18.53	4.6	160	312	75
-115.368	32.353	16.02	0	19.33	7	160	312	75
-115.391	32.371	16.02	0	20.29	1.4	160	312	75
-115.415	32.389	16.02	80	22.1	8.6	-100	312	75
-115.439	32.407	16.02	160	23.12	8.6	-100	312	75
-115.463	32.425	16.02	180	24.2	7.8	-100	312	75
-115.486	32.443	16.02	0	25.67	2.2	160	312	75
-115.51	32.461	16.02	0	23.98	1.4	160	312	75
-115.534	32.479	16.02	60	26.86	3.8	-100	312	75
-115.558	32.498	16.02	0	27.98	7	160	312	75
-115.581	32.516	16.02	20	30.01	6.2	-100	312	75
-115.605	32.534	16.02	0	30.28	8.6	160	312	75
-115.629	32.552	16.02	0	29.7	7.8	160	312	75
-115.652	32.57	16.02	20	32.61	2.2	-100	312	75
-115.676	32.588	16.02	100	34.91	8.6	160	312	75
-115.291	32.304	18.92	0	20.07	1.4	160	312	75
-115.315	32.322	18.92	0	19.41	8.6	160	312	75
-115.338	32.34	18.92	0	20.67	7.8	160	312	75
-115.362	32.358	18.92	0	20.45	6.2	160	312	75

-115.386	32.376	18.92	0	21.15	3	160	312	75
-115.41	32.394	18.92	0	22.97	5.4	160	312	75
-115.433	32.412	18.92	0	22.32	7	160	312	75
-115.457	32.43	18.92	0	24.93	7.8	160	312	75
-115.481	32.448	18.92	0	24.39	7	160	312	75
-115.505	32.467	18.92	0	24.49	2.2	160	312	75
-115.528	32.485	18.92	0	26.68	3	160	312	75
-115.552	32.503	18.92	0	28.1	7	160	312	75
-115.576	32.521	18.92	0	28.78	7.8	160	312	75
-115.599	32.539	18.92	0	30.28	7	160	312	75
-115.623	32.557	18.92	0	32.89	2.2	160	312	75
-115.647	32.575	18.92	0	31.13	1.4	160	312	75
-115.671	32.593	18.92	120	31.74	3	-100	312	75

Fault_segment = 3 nx(along strike)= 22 Dx= 3.00km ny(down dip)= 7 Dy= 3.00km

-115.329	32.274	1.38	0	13.25	7.8	160	131	60
-115.305	32.256	1.38	20	14.59	3.8	160	131	60
-115.281	32.238	1.38	80	15.88	1.4	160	131	60
-115.257	32.221	1.38	140	17.77	7	-112.5	131	60
-115.232	32.203	1.38	100	19.21	3.8	-125	131	60
-115.208	32.185	1.38	120	20.33	5.4	-162.5	131	60
-115.184	32.167	1.38	140	20.47	3.8	178.75	131	60
-115.16	32.15	1.38	180	21.09	6.2	-150	131	60
-115.136	32.132	1.38	60	22.55	2.2	-150	131	60
-115.112	32.114	1.38	40	22.71	1.4	-168.75	131	60
-115.088	32.096	1.38	20	27.87	7	178.75	131	60
-115.064	32.079	1.38	40	30	5.4	-168.75	131	60
-115.04	32.061	1.38	60	30.06	1.4	-143.75	131	60
-115.016	32.043	1.38	20	32.19	1.4	160	131	60
-114.992	32.026	1.38	40	30.75	2.2	160	131	60
-114.967	32.008	1.38	20	32.69	6.2	-175	131	60
-114.943	31.99	1.38	40	30.75	1.4	166.25	131	60
-114.919	31.973	1.38	80	33.09	3.8	160	131	60
-114.895	31.955	1.38	0	37.45	5.4	160	131	60
-114.871	31.937	1.38	0	40.85	3.8	160	131	60
-114.847	31.919	1.38	0	37.4	8.6	160	131	60
-114.823	31.902	1.38	0	45	7.8	160	131	60
-115.339	32.264	3.98	160	14.04	1.4	-175	131	60
-115.315	32.246	3.98	160	15.35	1.4	178.75	131	60
-115.291	32.228	3.98	100	16.39	8.6	-162.5	131	60
-115.267	32.21	3.98	120	17.52	3	-131.25	131	60
-115.243	32.193	3.98	140	19.08	8.6	-175	131	60
-115.219	32.175	3.98	200	20.45	8.6	-162.5	131	60
-115.195	32.157	3.98	240	20.55	6.2	-150	131	60
-115.171	32.139	3.98	300	22.43	6.2	-137.5	131	60
-115.147	32.122	3.98	260	21.7	7	-143.75	131	60
-115.122	32.104	3.98	200	24.16	4.6	178.75	131	60
-115.098	32.086	3.98	260	26.28	3	-168.75	131	60
-115.074	32.069	3.98	280	27.57	7.8	-175	131	60
-115.05	32.051	3.98	220	28.3	7.8	-168.75	131	60
-115.026	32.033	3.98	300	27.04	4.6	-168.75	131	60
-115.002	32.016	3.98	600	29.62	7	-162.5	131	60
-114.978	31.998	3.98	700	35.12	5.4	-162.5	131	60
-114.954	31.98	3.98	460	31.35	1.4	178.75	131	60
-114.93	31.962	3.98	340	31.32	3.8	160	131	60
-114.906	31.945	3.98	160	33.62	5.4	160	131	60
-114.881	31.927	3.98	60	38.82	3.8	160	131	60
-114.857	31.909	3.98	80	41.2	6.2	160	131	60
-114.833	31.892	3.98	30	42.59	3.8	160	131	60
-115.35	32.253	6.57	80	14.7	4.6	-143.75	131	60
-115.326	32.236	6.57	80	15.03	3.8	160	131	60
-115.302	32.218	6.57	80	17.2	1.4	160	131	60
-115.278	32.2	6.57	120	18.21	8.6	160	131	60

-115.253	32.182	6.57	140	19.48	8.6	160	131	60
-115.229	32.165	6.57	140	20.47	7	160	131	60
-115.205	32.147	6.57	120	21.1	7	160	131	60
-115.181	32.129	6.57	120	23.04	8.6	-156.25	131	60
-115.157	32.112	6.57	140	24.35	3	-175	131	60
-115.133	32.094	6.57	140	23.95	3.8	160	131	60
-115.109	32.076	6.57	180	27.53	8.6	-175	131	60
-115.085	32.058	6.57	200	26.72	1.4	-168.75	131	60
-115.061	32.041	6.57	160	29.62	7	-162.5	131	60
-115.037	32.023	6.57	220	32.4	3.8	-137.5	131	60
-115.012	32.005	6.57	440	28.69	7.8	-156.25	131	60
-114.988	31.988	6.57	480	36.19	1.4	-162.5	131	60
-114.964	31.97	6.57	200	33.4	7	-125	131	60
-114.94	31.952	6.57	40	39.17	6.2	-106.25	131	60
-114.916	31.934	6.57	0	38.53	3.8	160	131	60
-114.892	31.917	6.57	80	39.92	8.6	160	131	60
-114.868	31.899	6.57	80	34.6	3	160	131	60
-114.844	31.881	6.57	30	42.68	4.6	160	131	60
-115.36	32.243	9.17	60	16.56	3.8	-100	131	60
-115.336	32.225	9.17	40	17.01	5.4	-112.5	131	60
-115.312	32.208	9.17	40	18.12	3	160	131	60
-115.288	32.19	9.17	100	18.94	8.6	160	131	60
-115.264	32.172	9.17	100	20.1	8.6	160	131	60
-115.24	32.154	9.17	100	21.32	8.6	160	131	60
-115.216	32.137	9.17	80	21.85	7	160	131	60
-115.192	32.119	9.17	40	23.05	6.2	160	131	60
-115.168	32.101	9.17	60	24.27	2.2	-156.25	131	60
-115.143	32.084	9.17	100	23.19	3.8	160	131	60
-115.119	32.066	9.17	140	24.22	2.2	-156.25	131	60
-115.095	32.048	9.17	120	25.64	3.8	-143.75	131	60
-115.071	32.031	9.17	100	27.16	7.8	-131.25	131	60
-115.047	32.013	9.17	140	27.79	5.4	-100	131	60
-115.023	31.995	9.17	160	28.39	4.6	-131.25	131	60
-114.999	31.977	9.17	200	36.42	8.6	-156.25	131	60
-114.975	31.96	9.17	100	37.89	8.6	-112.5	131	60
-114.951	31.942	9.17	40	31.55	7	-100	131	60
-114.927	31.924	9.17	0	34.54	6.2	160	131	60
-114.902	31.907	9.17	160	41.17	8.6	160	131	60
-114.878	31.889	9.17	220	40.41	8.6	160	131	60
-114.854	31.871	9.17	30	42.84	4.6	160	131	60
-115.371	32.233	11.77	140	17.95	8.6	-100	131	60
-115.347	32.215	11.77	40	18.45	1.4	-100	131	60
-115.323	32.197	11.77	0	18.25	1.4	160	131	60
-115.298	32.18	11.77	40	19.86	8.6	160	131	60
-115.274	32.162	11.77	100	20.89	8.6	-162.5	131	60
-115.25	32.144	11.77	100	21.01	8.6	-162.5	131	60
-115.226	32.127	11.77	100	22.8	3	166.25	131	60
-115.202	32.109	11.77	120	23.57	2.2	-156.25	131	60
-115.178	32.091	11.77	80	23.91	3.8	160	131	60
-115.154	32.074	11.77	160	23.54	4.6	-175	131	60
-115.13	32.056	11.77	180	25.3	7.8	-168.75	131	60
-115.106	32.038	11.77	180	28.94	6.2	178.75	131	60
-115.082	32.02	11.77	140	30.22	3	178.75	131	60
-115.058	32.003	11.77	120	28.55	1.4	-162.5	131	60
-115.033	31.985	11.77	60	34.39	3	-106.25	131	60
-115.009	31.967	11.77	100	30.74	1.4	178.75	131	60
-114.985	31.95	11.77	80	31.26	1.4	160	131	60
-114.961	31.932	11.77	80	39.66	7	-156.25	131	60
-114.937	31.914	11.77	120	38	8.6	-100	131	60
-114.913	31.896	11.77	180	41.42	5.4	160	131	60
-114.889	31.879	11.77	240	40.63	7.8	160	131	60
-114.865	31.861	11.77	30	41.95	2.2	-137.5	131	60
-115.381	32.223	14.37	100	19.65	3.8	-100	131	60

-115.357	32.205	14.37	40	18.51	2.2	-100	131	60
-115.333	32.187	14.37	20	20.1	8.6	160	131	60
-115.309	32.17	14.37	40	21.6	8.6	-100	131	60
-115.285	32.152	14.37	80	21.82	4.6	-125	131	60
-115.261	32.134	14.37	80	21.45	4.6	-131.25	131	60
-115.237	32.116	14.37	100	23.12	5.4	160	131	60
-115.213	32.099	14.37	140	25.1	8.6	-175	131	60
-115.188	32.081	14.37	120	23.36	5.4	160	131	60
-115.164	32.063	14.37	180	26.97	7.8	-175	131	60
-115.14	32.046	14.37	180	25.33	1.4	178.75	131	60
-115.116	32.028	14.37	180	26.77	3.8	160	131	60
-115.092	32.01	14.37	160	26.92	3	160	131	60
-115.068	31.992	14.37	140	27.93	3	-162.5	131	60
-115.044	31.975	14.37	100	30.53	3	178.75	131	60
-115.02	31.957	14.37	160	37.14	7	160	131	60
-114.996	31.939	14.37	160	38.58	7	172.5	131	60
-114.972	31.922	14.37	120	38.94	5.4	178.75	131	60
-114.947	31.904	14.37	100	39.29	7	-118.75	131	60
-114.923	31.886	14.37	140	41.73	2.2	172.5	131	60
-114.899	31.869	14.37	160	41.98	3.8	-150	131	60
-114.875	31.851	14.37	30	39.29	4.6	-100	131	60
-115.392	32.212	16.97	80	20.77	6.2	-100	131	60
-115.368	32.195	16.97	0	19.41	8.6	160	131	60
-115.344	32.177	16.97	0	19.19	3	160	131	60
-115.319	32.159	16.97	0	22.4	7.8	160	131	60
-115.295	32.142	16.97	0	20.37	7	160	131	60
-115.271	32.124	16.97	0	22.97	6.2	160	131	60
-115.247	32.106	16.97	0	24.35	8.6	160	131	60
-115.223	32.089	16.97	0	23.72	5.4	160	131	60
-115.199	32.071	16.97	0	26.49	5.4	160	131	60
-115.175	32.053	16.97	0	26.58	1.4	160	131	60
-115.151	32.035	16.97	0	26.68	3.8	160	131	60
-115.127	32.018	16.97	0	26.8	4.6	160	131	60
-115.103	32	16.97	0	32.65	7	160	131	60
-115.078	31.982	16.97	0	29.85	6.2	160	131	60
-115.054	31.965	16.97	0	35.3	4.6	160	131	60
-115.03	31.947	16.97	0	31.42	1.4	160	131	60
-115.006	31.929	16.97	0	33.81	7	160	131	60
-114.982	31.911	16.97	0	36.53	3.8	160	131	60
-114.958	31.894	16.97	0	36.1	1.4	160	131	60
-114.934	31.876	16.97	0	39	4.6	160	131	60
-114.91	31.858	16.97	0	43.5	7	160	131	60
-114.886	31.841	16.97	30	43.67	3.8	160	131	60

Fault_segment = 4 nx(along strike)= 6 Dx= 3.00km ny(down dip)= 6 Dy= 3.00km

-115.721	32.579	1.38	90	31.29	1.4	-163.12	335	50
-115.734	32.603	1.38	60	33.27	2.2	-151.88	335	50
-115.748	32.627	1.38	40	39.27	7.8	-174.38	335	50
-115.761	32.652	1.38	0	40.64	7.8	160	335	50
-115.775	32.676	1.38	0	37.19	1.4	160	335	50
-115.788	32.701	1.38	15	40.28	2.2	-100	335	50
-115.702	32.586	3.68	140	33.63	7.8	-100	335	50
-115.716	32.61	3.68	220	37.26	8.6	-100	335	50
-115.729	32.635	3.68	40	36.62	5.4	-100	335	50
-115.743	32.659	3.68	0	35.53	1.4	160	335	50
-115.756	32.684	3.68	0	37.81	7.8	160	335	50
-115.77	32.708	3.68	0	37.21	3	160	335	50
-115.683	32.593	5.98	0	35.42	7.8	160	335	50
-115.697	32.618	5.98	0	36.08	1.4	160	335	50
-115.711	32.642	5.98	80	37.99	8.6	160	335	50
-115.724	32.667	5.98	20	39.28	3	-100	335	50
-115.738	32.691	5.98	100	42.12	3	-150	335	50
-115.751	32.716	5.98	15	41.85	2.2	160	335	50

-115.665	32.601	8.27	100	32.9	8.6	-100	335	50
-115.678	32.625	8.27	60	34.54	3.8	-100	335	50
-115.692	32.65	8.27	40	35.7	4.6	-100	335	50
-115.705	32.674	8.27	0	36.29	7	160	335	50
-115.719	32.698	8.27	0	40.71	3.8	160	335	50
-115.732	32.723	8.27	15	39.18	1.4	-100	335	50
-115.646	32.608	10.57	40	32.19	3	-100	335	50
-115.66	32.632	10.57	0	33.73	2.2	160	335	50
-115.673	32.657	10.57	0	37.71	8.6	160	335	50
-115.687	32.681	10.57	0	37.05	6.2	160	335	50
-115.7	32.706	10.57	40	40.19	8.6	-100	335	50
-115.714	32.73	10.57	0	38.13	1.4	160	335	50
-115.627	32.615	12.87	100	32.91	3.8	-100	335	50
-115.641	32.64	12.87	0	33.51	2.2	160	335	50
-115.655	32.664	12.87	0	36.74	5.4	160	335	50
-115.668	32.689	12.87	0	35.64	3	160	335	50
-115.682	32.713	12.87	0	38.44	2.2	160	335	50
-115.695	32.738	12.87	30	42.44	3	-100	335	50